Christiane Mellak, BSc

Rotary Anode Drive for X-ray Tubes

MASTER'S THESIS

to achieve the university degree of

Diplom-Ingenieurin

Master's degree programme: Biomedical Engineering

submitted to
Graz University of Technology

Supervisors
Univ.-Prof. Dipl.-Ing. Dr.techn. Baumgartner Christian
Ass.Prof. Dipl.-Ing. Dr.techn. Krischan Klaus

Institute for Health Care Engineering

Graz, June 2017

Statutory Declaration

I declare that I have authored this thesis independently, that I have not used other than the declared sources/resources, and that I have explicitly indicated all material which has been quoted either literally or by content from the sources used. The text document uploaded to TUGRAZonline is identical to the present master's thesis.

Graz, _____ _____

Date Signature

Abstract

This thesis investigates the replacement of an existing X-ray tube induction machine rotor with that of a synchronous reluctance machine. The feasibility of simple rotor replacement was investigated by finding synchronous reluctance machine rotor shapes capable of providing the same torque output as the original induction machine rotor in combination with the original stator. Using 2D-Finite Element Analysis software JMAG (JSOL Corporation), characterising parameters of three appropriate synchronous reluctance machine rotors were found and the rotor and stator losses of the synchronous reluctance machines are compared to the losses of the original induction machine. From the rotors studied in this thesis, the most promising is an axially-layered rotor which showed more than 50% reduction of total losses for the same torque output. Considerations for future work include ensuring compatibility with the X-ray tube vacuum environment.

Contents

List of Symbols and Abbreviations

Abbreviations

FEA	**F**inite **E**lement **A**nalysis
IM	**I**nduction **M**otor
SRM	**S**ynchronous **R**eluctance **M**otor
MTC	**M**aximum **T**orque **C**ontrol
MTPA	**M**aximum **T**orque **P**er **A**mpere
MPFC	**M**aximum **P**ower **F**actor **C**ontrol

Symbols

p	Number of pole pairs
L_{q}	q-axis inductance, including leakage inductance
L_{d}	d-axis inductance, including leakage inductance
L_{qm}	q-axis magnetizing inductance
L_{dm}	d-axis magnetizing inductance
β	Machine current angle
$\beta_{\mathrm{PF}_{\mathrm{max}}}$	Machine current angle for maximum power factor
$\beta_{T_{\mathrm{max}}}$	Machine current angle for maximum torque output

α	Angle between U-phasor and d-axis
ϕ_s	Phase shift between stator current and voltage phasor
U_{ds}, U_{qs}	Stator voltage in d-axis/q-axis
$\bar{U}_{ph}$	Stator per phase voltage peak value
i_s	Stator phase current
$\underline{I}_s$	Stator per phase current phasor (peak value)
$\underline{U}_s$	Stator per phase voltage phasor (peak value)
$\underline{\lambda}_s$	Stator per phase flux linkage phasor (peak value)
i_{ds}, i_{qs}	Stator terminal current in d-axis/q-axis
i_d, i_q	Stator magnetizing current in d-axis/q-axis
i_{dm}, i_{qm}	d-axis/q-axis magnetizing current
λ_{ds}, λ_{qs}	d-axis/q-axis stator flux linkage
λ_{dm}, λ_{qm}	d-axis/q-axis magnetizing flux linkage
R_S	Stator per phase resistance
$R_{S,20\,°C}$	Stator per phase resistance at 20 °C
$R_{S,60\,°C}$	Stator per phase resistance at 60 °C
R_{m1}	Equivalent stator iron loss resistance
R_{m2}	Equivalent rotor iron loss resistance
$L_{s\sigma}$	Stator per phase leakage inductance
ω_r	Electrical angular velocity
ξ	Saliency Ratio
ζ	Torque Index
T_{avg}	Average Torque

$P_{\text{Cu,Stator}}$	Stator copper losses
$P_{\text{Fe,Stator}}$	Stator iron losses
$P_{\text{Cu,Rotor}}$	Rotor copper losses
$P_{\text{Fe,Rotor}}$	Rotor iron losses
$P_{\text{Cu,Rotor,layer}}$	Rotor copper layer losses
$P_{\text{v,mech}}$	Mechanical losses
P_{misc}	Additional losses
$P_{\text{el,total}}$	Total electric power / Input power
P_{mech}	Mechanical power / Output power
PF_{ϕ_s}	Power factor calculated with ϕ_s
PF	Power factor calculated using (1.9)
ρ	Electric resistivity
ρ_{20}	Electric resistivity at 20 °C
$\rho_{\text{Cu,60°C}}$	Electric resistivity of copper at 20 °C
$\rho_{\text{SM,400°C}}$	Electric resistivity of sheet metal 50H600 at 400 °C
α_t	Temperature coefficient
ΔT	Temperature change
$I_{\text{ph,rms}}$	RMS value of phase current
$u_{\text{ph}}(t)$	Phase voltage time dependent
$i_{\text{ph}}(t)$	Phase current time dependent
J	Current density
Δt	Sampling intervall
n	Rotational speed

n_s	Synchronous speed
s	Slip

1 Introduction

Induction motors are the most common drives in modern X-ray tubes for medical applications. Considering the well studied advantages and disadvantages of induction motors currently in use for general radiography, this work proposes replacing the rotor of an induction motor (IM) with that of a synchronous reluctance motor (SRM). The aim is to minimize losses caused by the drive to give room for increased X-ray beam power yet meeting the same minimum requirements of start-up time and torque. This work presents a general feasibility study of three different SRM rotors placed in the stator of an existing market-ready X-ray tube IM by applying the 2-D Finite Element Method (FEM). Furthermore losses and loss distribution of the IM and the SRMs are compared.

1.1 Motivation

Throughout the last century, X-ray tubes have been subject to extensive research and major developments have been made including reduced losses, improved control, increased power density and intensity all with regards to high quality X-ray images [1], [2], [3, p. 1-29]. However, to the present day the melting point of the materials in use remains one of the main limiting factors for the X-ray beam power, limiting achievable image quality. It follows that reducing heat generation within the vacuum compartment of an X-ray tube gives room for increased electron beam power and X-ray tube power respectively. [3, p. 187; 234]

In other motor applications, a popular alternative to the IM is the permanent magnet synchronous motor. However, the sintered magnetic materials utilized by such motors (e.g. ferrite, rare earth magnets) cause difficulties

with the long term stability of the vacuum and, furthermore, the likelihood of demagnetization increases with temperature [4]. This rules out any permanent magnet assisted drives as a viable alternative. Thus, a synchronous reluctance drive is a good alternative because of its ruggedness and construction simplicity, the absence of rotor winding losses and a very good compatibility with the power electronic converter [5].

A distinguishing characteristic of a drive in such an application is a notably large air gap compared to other drives (Section 1.2)[3, p.273]. Though, no specific literature could be found dealing with the influence of a synchronous reluctance machine's large air gap on machine performance, various literature exists that does investigate induction/synchronous machine rotor replacement. As such, the main approach of this thesis - replacement of the rotor of an IM with that of a synchronous reluctance machine - can be justified as follows:

- By comparing a squirrel cage IM to a SRM, it can be shown by means of analysis that around 80% of the torque can be retained for 50% of the loss [6].

- Even though for the same output torque, the IM requires lower current than the SRM, the total joule losses are greater because of the required current flowing in the rotor.

- The rotor replacement implicates a transfer of rotor losses to stator copper losses restricted only by the limited thermal dissipation of stator winding end connections [7]. This is highly desirable considering the construction of an X-ray tube (Section 1.2) and the much easier access to, and cooling of, the stator.

Due to the high rotational speed the drive is powered by a frequency converter. Although control of the drive is not covered in this thesis a few general advantages of converter-fed synchronous reluctance drives shall be pointed out here [5]:

- There is no need for a starting cage, thus it is possible to design the rotor purely for synchronous performance.

- An optimum torque angle at all loads and speeds can be ensured with electronic control making pull out unlikely.

- There is no need for a damper winding. Power density is increased by designing the rotor for the highest possible reactance difference $X_d - X_q$.

On the downside converter fed drives suffer from additional losses caused by higher harmonics generated by the converter [5] and a sensorless rotor position estimation (as shown in [8]–[10]) is needed to ensure high performance [6].

1.2 Background

This section gives a brief introduction to X-ray generation based on an exemplary rotating anode tube and basic synchronous reluctance principles with respect to the carried out simulations.

X-ray Generation

The interior of a modern X-ray tube used for standard medical application, such as general radiography, consists of a negatively charged cathode and a positively charged anode. A coil of tungsten wire ("filament") functions as the cathode. It is heated by low voltage to expel electrons from the filament by a process called "thermionic emission". The expelled electrons are then accelerated by high voltage (up to 150 kV) and hit the anode on a well sized target area with a specific kinetic energy. Consequently, X-rays (also called "Bremsstrahlung") are produced due to electron interactions [3, p. 31-80]. To avoid any interaction between the accelerated electrons on their way to the anode and foreign molecules the electrodes must be placed in a vacuum. [11] As the electrons hit the target area, around 60 % of the electrons energy is converted to heat and 39 % of the energy is lost through backscattered electrons. The remaining 1 % is reduced by radiation shielding, leaving 0.03 % for the useful collimated X-ray beam. [3, p. 35] This unavoidable heat

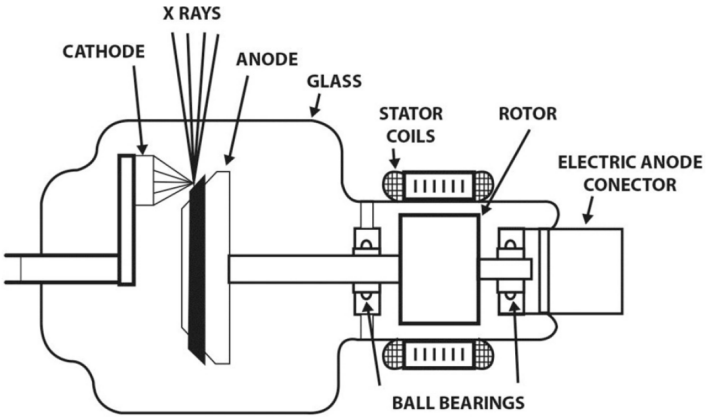

Fig. 1.1: X-ray tube assembly with major components [12].

generation is one of the main limiting factors in modern X-ray tubes and consequently the majority of applications use a rotating anode assembly as shown in Fig. 1.1 rather than a stationary anode. In a rotating assembly, the thermal energy produced is spread over a larger area resulting in higher X-ray output capability.

Thereby the envelope holding the vacuum separates rotor and stator of the necessary drive (Fig. 1.1 shows a glass envelope) resulting in a larger air gap (its size ranging between 3 mm and 12 mm depending on the type of tube) than usually preferred in electric drives. The reference IM for this thesis is a component of a bipolar glass tube. This means the anode (-75 kV) must be separated from the stator (ground potential) by an additional isolation layer due to the high potential difference between stator and rotor (connected to the high voltage circuit) leading to an air gap of around 8 mm, adding to the complexity of the assembled drive [3, p. 273][13, p. 89].

To remove heat from the assembly, the envelope is surrounded by isolating cooling oil (not shown in Fig. 1.1) whereas the only way to cool the parts located inside the vacuum compartment is by radiative emission. The rotor of the drive and the rotating anode are connected through a molybdenum stem because molybdenum is a very poor heat conductor and prevents heat transfer from the anode to the bearings. This is especially important because bearings are heat sensitive and their overheating often leads to X-ray tube

failure. Emphasizing once again the importance of minimizing the heat generation in the moving part of the drive. [13, p. 99]

To give an impression of the heat created in an X-ray tube, some general operating temperatures are listed in Table 1.1.

Component	Value
Anode	1500 °C
Rotor	< 450 °C
Stator	< 60 °C

Table 1.1: Temperatures of different components in X-ray tubes [14].

Synchronous Reluctance Principles

To obtain a sufficient understanding of the synchronous reluctance machine, the well known analytical model is presented here [5], [15]. A synchronous reluctance machine develops torque only through differing values of reluctance in the d (*direct*) -axis compared to the q (*quaradature*) -axis direction (Fig. 1.3). An energized system tends to minimise the energy stored in the magnetic field, hence, if the field is constantly rotating around a salient piece of magnetizable metal (the rotor), constant reluctance torque is generated (in the ideal case) under the assumption that the angle between rotor and magnetic field is fixed.

A simplified equivalent circuit in rotor reference frame is introduced here and a few assumptions are made:

- R_{m1} accounts for the main flux core losses in the stator iron and is neglected here due to the fact that it has very little effect on the torque output. Nevertheless it will be accounted for in post-processing. Thus, $i_{d,Fe,S} = 0$ and likewise $i_{q,Fe,S} = 0$.
- R_{m2} accounts for the main flux core losses in the rotor iron and is neglected for the analytical model due to the fact that it has very little effect on the torque output. Nevertheless it will be accounted for during the simulation. Thus, $i_{d,Fe,R} = 0$ and likewise $i_{q,Fe,R} = 0$.

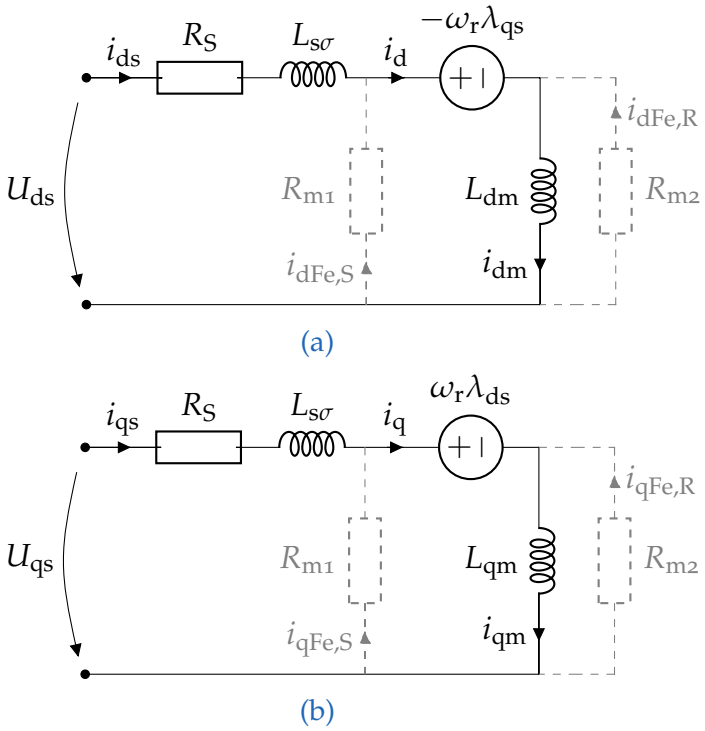

Fig. 1.2: Synchronous reluctance equivalent circuits in rotor reference frame: d-axis (a) and q-axis (b).

- R_{m1} and R_{m2} are neglected, consequently $i_{ds} = i_d = i_{dm}$ and $i_{qs} = i_q = i_{qm}$.
- The magnetizing inductances were not extracted in this thesis. Thus, $L_d = L_{dm} + L_{s\sigma}$ and $L_q = L_{qm} + L_{s\sigma}$.

After making the stated assumptions the equations modelling the synchronous reluctance machine in reference to the equivalent circuits shown in Fig. 1.2 can be introduced:

$$U_{ds} = R_s i_{ds} + L_{s\sigma}\frac{di_{ds}}{dt} - \omega_r\lambda_{qs} + \frac{d\lambda_{dm}}{dt} \tag{1.1}$$

$$U_{qs} = R_s i_{qs} + L_{s\sigma}\frac{di_{qs}}{dt} + \omega_r\lambda_{ds} + \frac{d\lambda_{qm}}{dt} \tag{1.2}$$

U_{ds}, U_{qs} = Stator voltage in d-axis/q-axis
i_{ds}, i_{qs} = Stator terminal current in d-axis/q-axis
i_{dm}, i_{qm} = d-axis/q-axis magnetizing current
λ_{ds}, λ_{qs} = d-axis/q-axis stator flux linkage
λ_{dm}, λ_{qm} = d-axis/q-axis magnetizing flux linkage
R_s = Stator per phase resistance
R_{m1} = Equivalent stator iron loss resistance
R_{m2} = Equivalent rotor iron loss resistance
$L_{s\sigma}$ = Stator per phase leakage inductance
ω_r = Electrical angular velocity

With following relations (1.3) and (1.4) the torque expression in the common *d-q* axis theory is given in (1.5).

$$\lambda_{ds} = L_{s\sigma} i_{ds} + L_{dm} i_{dm} \tag{1.3}$$

$$\lambda_{qs} = L_{s\sigma} i_{qs} + L_{qm} i_{qm} \tag{1.4}$$

$$T = \frac{3p}{2}(\lambda_{ds} i_{qm} - \lambda_{qs} i_{dm}) \tag{1.5}$$

Using simple trigonometry, torque can alternatively expressed as:

$$T = \frac{3p}{4}(L_d - L_q) i_s^2 \sin(2\beta) \tag{1.6}$$

p = number of pole pairs
L_{qm} = q-axis magnetizing inductance
L_{dm} = d-axis magnetizing inductance
L_q = q-axis inductance, including leakage inductance
L_d = d-axis inductance, including leakage inductance
i_s = stator phase current
β = machine current angle

Equation (1.6) shows that with fixed stator current i_s maximum torque can be reached with a machine current angle β (angle between current vector and d-axis of the machine) of 45°.

Two figures of merit are important when addressing the performance of a synchronous reluctance machine: the saliency ratio ξ (1.7) and the torque index ζ (1.8). The former gives information about the anisotropic magnetic reluctance ratio of the rotor, which is directly linked to the power factor and the phase current of the machine. The latter indicates the torque capability of the machine. Note that the true saliency ratio of the synchronous reluctance machine includes leakage inductance $L_{s\sigma}$ [15].

$$\xi = \frac{L_d}{L_q} \tag{1.7}$$

$$\zeta = (L_{dm} - L_{qm}) \tag{1.8}$$

By these key indicators it can be shown that for a rotor design with competitive power factor and torque production, the d-axis inductance must be maximized and the q-axis inductance must be minimized. [16]

Note that due to the finite value of R_{m1}, a phase shift between the stator current and MMF occurs. Therefore to obtain maximum torque, the actual current vector β is significantly higher than predicted by the linear lossless model [5], [18]. Another important aspect that is ignored here is the effect of cross-coupling and the different saturation in d-axis and q-axis. This causes discrepancies between the linear model and the actual machine [15], but is beyond the scope of this introduction. Nonetheless, these effects are observable in the simulations presented in this thesis.

To provide a sufficient analysis a few further equations are introduced [19]:

Neglecting the stator resistance R_{m1}, the power factor $\cos\phi$ for every value of β can be calculated using (1.9).

$$PF = \frac{\xi - 1}{\sqrt{\xi^2 \frac{1}{\sin^2\beta} + \frac{1}{\cos^2\beta}}} \tag{1.9}$$

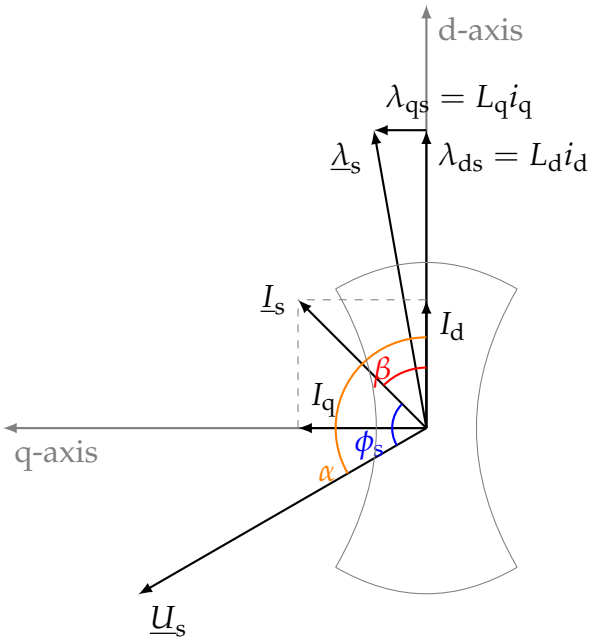

Fig. 1.3: Vector diagram of a synchronous reluctance machine for the simplified model in dq-reference frame [17].

According to equation (1.9) the value reaches its maximum when β is equal to:

$$\beta_{\mathrm{PF}_{\max}} = \arctan(\sqrt{\xi}) = \arctan\sqrt{\frac{L_\mathrm{d}}{L_\mathrm{q}}} \tag{1.10}$$

Note that $\beta_{PF_{\max}}$ and β for maximum torque output $\beta_{T_{\max}}$ do not necessarily match.

Neglecting R_{m1} leads to much lower power factors when compared to the power factor calculated with the actual phase angle between current and voltage (1.11)

$$PF_{\phi_\mathrm{s}} = \cos\phi_\mathrm{s} \tag{1.11}$$

Losses

This section provides an overview of the different types of losses occurring in an electrical machine. To visualize typical energy flow of a machine the power flow diagram for an IM is shown in Fig. 1.4. Each type of loss is briefly discussed here including differences to synchronous reluctance machines [18, pp. 193 ;458] [20, pp. 9-1]:

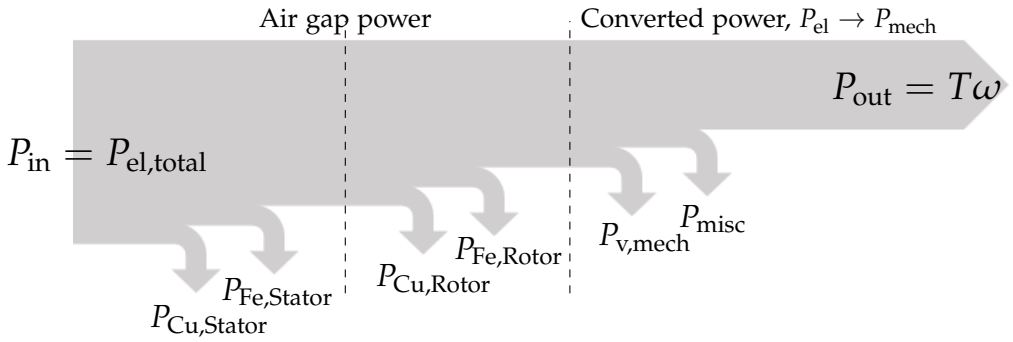

Fig. 1.4: Power flow of an IM. [21, p.394]

Copper Losses/Resistive Losses: These occur in rotor conductors (if present) and stator windings and depend on the resistivity of the material, the current density in the material and its volume. While some $P_{Cu,Rotor}$ losses occur in the IM, the copper losses in the rotor of the SRM are zero as no currents flow in the rotor.

$$P_{Cu} = P_{Cu,Stator}(+P_{Cu,Rotor})$$

Iron Losses: Consist of eddy current and hysteresis losses. Eddy currents arise in magnetically and electrically conductive material and occur as a result of induced voltages caused by variations in flux-density. Hysteresis losses occur in magnetically conductive material. The energy loss per cycle is proportional to the enclosed area of the B-H loop, hence the average power loss due to hysteresis is dependent on the frequency of the variation in the magnetic field. In ideal synchronous (reluctance) machines, the rotor iron losses are zero as the rotor rotates at synchronous speed and thus no magnetic field modulation is seen

by the rotor. Nevertheless, rotor losses are incurred because higher frequency asynchronous waves rotate at different speeds to the main flux. This is primarily caused by the stator slots, the non-uniform winding distribution, and salient rotor shapes [15]. Iron losses will not be divided into its constituent components, but rather a total value will be obtained by FEA-simulation.

$$P_{\mathrm{Fe}} = P_{\mathrm{Fe,Stator}} + P_{\mathrm{Fe,Rotor}}$$

Mechanical Losses: Rotors running at higher speed usually have to overcome higher air resistance leading to significant higher air friction losses [22], considering the vacuum environment of the rotor mechanical losses are reduced to ball bearing friction losses in the considered case and are neglected.

$$P_{\mathrm{v,mech}} = 0$$

Additional Losses: These losses are all electromagnetic losses which are not included in copper and iron losses already mentioned, for example losses caused by the skin effect in conductors or load-depended losses. They are considered to be very difficult to calculate and measure and only responsible for a small percentage of the total losses (e.g. 0.5% of input power in an IM). In this thesis these losses are included in the total iron losses and will not be extracted from the total value.

$$P_{\mathrm{misc}} = x\%P_{\mathrm{Fe}}$$

Generally spoken the air gap defines the main or magnetizing inductance and thus defines the stator current needed to create a certain magnetic field in the air gap. Therefore the size of the air gap heavily influences the resistive losses in the stator. Thus in standard machines it is desirable to make the air gap as small as possible. However, making the air gap too small results in higher losses on the surface of the rotor (this effect becomes highly relevant in a non-laminated rotor) due to non sinusoidal stator winding distribution and slot harmonics raising the idea that with a large air gap as in the investigated drive stator slot harmonics will have very little effect on the loss density in the rotor. [18] However, the large air gap leads to a higher magnetizing current increasing copper losses in the stator.

2 Problem Statement

A fundamental question at the beginning of this work was whether the required torque output can be reached relying solely on the reluctance principle, despite possible advantages or disadvantages of the IM. After carefully choosing promising rotor shapes and carrying out a FEA, a loss comparison at a given operating point was conducted. A thorough study on performance, torque capability and saliency ratio was performed on the SRMs.

This chapter starts with a few general assumptions made prior to the simulations as well as with a description of the basic drive requirements. Furthermore, the reference IM is specified and the three chosen reluctance rotors are introduced.

Assumptions

- The stator of the original induction machine (e.g. number of pole pairs, winding configuration, number of turns, etc.) will be used as this work focuses on a suitable rotor shape. Possible optimizations in the stator configuration will be left for further research.
- Rated speed and torque remain unchanged.
- Mechanical (e.g. evaluation of centrifugal forces, manufacturing, change of shaft diameter, etc.) and thermal (e.g. choice of material, etc.) viability will be left for further research.
- Possible can materials of X-ray tubes include stainless steel, metal, ceramics or as previously mentioned, glass. The investigated stator and rotor configuration assume a can made out of electrically non-conductive material. Every other case goes beyond the scope of this work and will be left for further research.

Drive requirements

The basic drive requirements are given in Table 2.1. Friction torque caused by the ball bearings or other factors such as the exact materials of the anode disc are unknown. Therefore a (rather conservative) estimation of the required torque of 1 Nm was made to ensure the anode reaches its required speed in an acceptable time.

Parameter	Value
Start-up time	$< 3\,\mathrm{s}$
Moment of Inertia	$\sim 0.0005\,\mathrm{kg\,m^2}$
Power	$\sim 170\,\mathrm{W}$
Rotational Speed	$180\,\mathrm{Hz}$
Torque T	$\sim 1\,\mathrm{N\,m}$

Table 2.1: Basic drive requirements.

A qualitative time sequence of the operating mode of the drive for the investigated X-ray tube is shown in Fig. 2.1. The investigated X-ray tube is used for standard or plain radiography which usually means short exposure times for a single X-ray image. When exposure is initiated the disc is accelerated to the required speed. After the boost time the stator enters run mode which indicates a reduction of the applied voltage to maintain minimum speed. After taking the shot, the disc needs to be braked actively to increase bearing live expectancy. [23]

Note that operating modes and, subsequently, various components such as bearings or housing material, vary significantly for various X-ray tube applications [24].

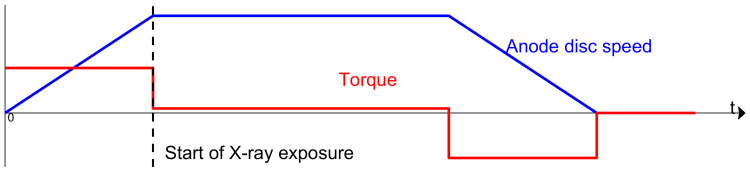

Fig. 2.1: Typical operating mode for single shot X-ray [24].

2.1 Specifications of Reference Induction Motor

One of the standard IMs for an x-ray tube assembly currently in use consists of a three phase two pole stator with a single-layer distributed winding. The rotor is constructed of a solid iron hollow cylinder covered with a thin coat of copper. The iron serves as the magnetic flux return path and the copper as the conductive layer. The main dimensions for the stator are given in Table 2.2 and for the rotor in Table 2.3. Fig. 2.2 shows the cross-section used for the 2D-FEM analysis with the corresponding components listed in 2.4.

Parameter	Value
Inner Radius	26.5 mm
Outer Radius	47.5 mm
Number of slots	24
Number of phases	3
Number of poles	2
Axial length	50 mm
Winding	single-layer distributed
No. of turns per slot	64
Phase resistance $R_{S,20\,°C}$	7.1 Ω
Voltage $\bar{U}_{ph}$	400 V_{ac}
Connection	Star

Table 2.2: Stator geometry and specifications.

Parameter	Value
Shaft Radius	14.5 mm
Yoke Radius	16 mm
Outer Radius	18.5 mm

Table 2.3: Rotor geometry.

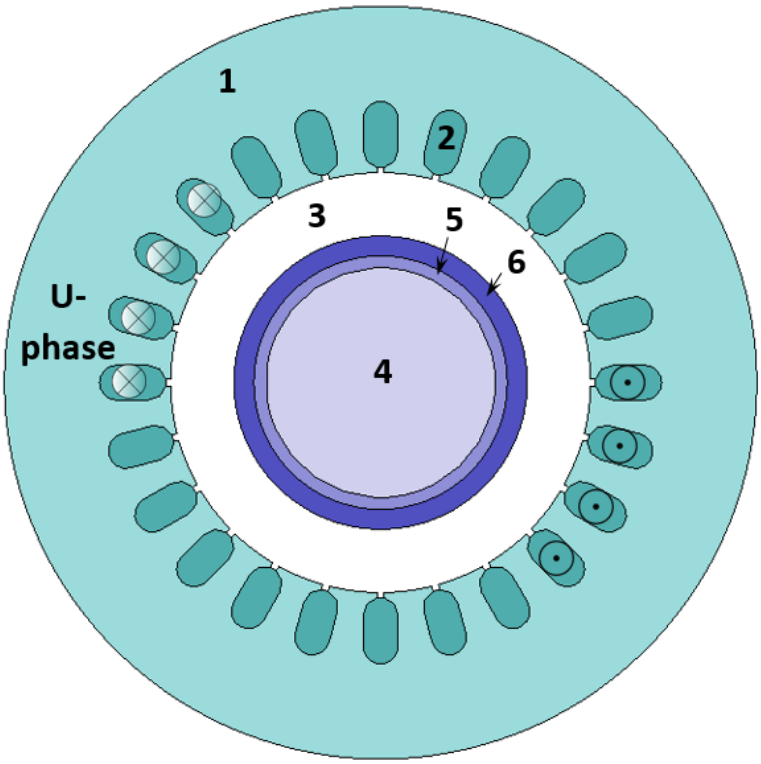

Fig. 2.2: Cross section of IM.

	Component	Material
1	Stator	Steel Sheet (50H600)
2	Coils	Copper
3	Air gap	-
4	Shaft	Air
5	Rotor yoke	Solid Steel (50H600)
6	Rotor conductive layer	Copper

Table 2.4: Components of IM.

2.2 Investigated SRM Rotor Shapes

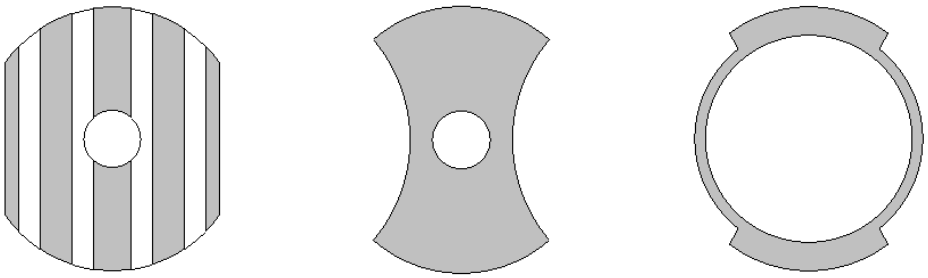

(a) (b) (c)

Fig. 2.3: Rotor designs for SRMs:
axially-layered (a), solid salient (b) and ring salient (c)

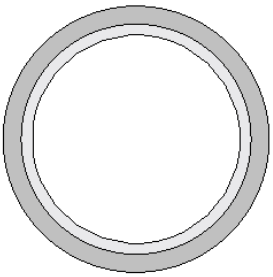

Fig. 2.4: Rotor of reference IM.

Given the required vacuum environment, the construction of the SRM rotor is critical. It can be challenging to find suitable rotor shapes for the specific requirements of an X-ray tube environment since most SRM rotor shapes found in literature are for a 4-pole stator configuration rather than 2-pole configuration [6], [16], [25]. This difficulty is compounded by the fact that every form of lamination leads to the risk of vacuum deterioration and X-ray tube failure.

In this work three rotor shapes were investigated and are shown in Fig 2.3. They are referred to herein as the axially-layered, solid salient and ring salient rotor. As a reference, the rotor of the induction machine is shown in Fig. 2.4. For the SRM rotors the q-axis is an imaginary horizontal line

cutting the rotors into upper and lower half, the d-axis is an imaginary vertical line dividing the rotors into right and left side.

Axially-layered Rotor

Fig. 2.3a shows an axially-layered rotor with alternating magnetic and non-magnetic layers. This type of rotor shows promising results [4], [26], [27] and should not be overlooked, however, compatibility of the layers with the vacuum environment has yet to be investigated.

Solid Salient Rotor

Fig. 2.3b shows a solid salient rotor as proposed in [4], [28], [29] and represents one of various "cut-out" rotor shapes ([28], [30]). Such rotors are easy to manufacture and are robust but circulating flux in the pole faces of the rotor do not allow high saliency ratios. [4]

Ring Salient Rotor

The ring salient rotor shown in Fig. 2.3c was chosen based on [4]. This rotor shape offers the most similar construction to the reference IM rotor allowing minimal reconfiguration of the overall tube construction.

3 Methods

This chapter covers whether and how the introduced boundary conditions were accounted for during the simulation. A detailed analysis of strength and weaknesses of the applied methods can be found in chapter 5.

Results are obtained by application of 2D non-linear transient Finite Element Analysis (FEA) as well as some analytical calculations.

The FEA was carried out with JMAG (JSOL Corporation). As an example the generated mesh for the solid salient rotor (Fig. 2.3b) is shown in Fig. 3.1. Generally, a very fine mesh should be used. However, in the interest of acceptable simulation duration a trade-off between accuracy and simulation time has to be made. To significantly reduce calculation time it is possible to take advantage of the rotational symmetry of a motor. For a 2-pole stator simulating only half of the model leads to the same results 3.1a.

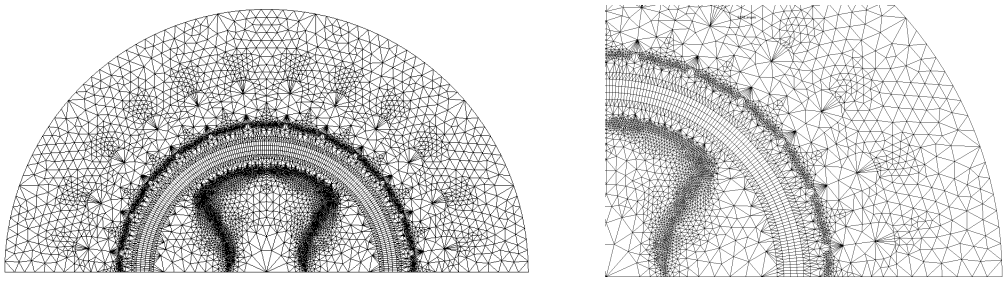

(a) (b)

Fig. 3.1: The half model mesh used for the simulation (a) and a closer look (b).

3.1 Material properties

All simulations are carried out using the same magnetic material provided by the JMAG material database. A relative comparison using the identical material will provide useful information about the general feasibility and loss distribution of the simulated rotor structures. The manufacturer of the used steel metal is the Nippon Steel Corporation, Japan and the material number is 50H600. This number indicates a core loss of 6 W/kg at 50 Hz and 1.5 T. The magnetization curve is shown in Fig. 3.2. It should also be noted that aluminium is used as the non-magnetic material for the axially-layered rotor (Fig. 2.3a) but, depending on different parameters such as mechanical strength and thermal conductivity, it can be substituted with any other kind of non-magnetic material. All relevant material properties are given in Table 3.1. The influence of temperature variation and the implemented changes made is treated in Section 3.2.

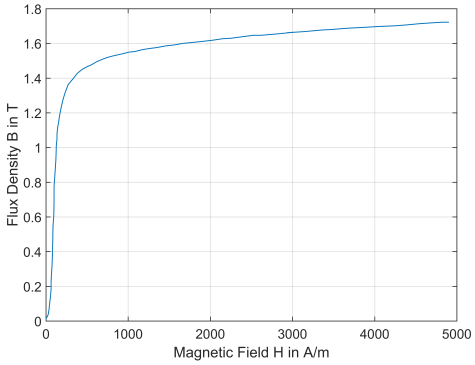

Fig. 3.2: BH-Curve of Magnetic Steel Sheet 50H600 taken from the JMAG Material Editor.

	Sheet Metal (SM)/Rotor (50H600)	Conductor (Copper)	Non-magnetic Material (Aluminium)
Electric Resistivity ρ_{20}	$3.2 \cdot 10^{-7}\,\Omega\,\mathrm{m}$	$1.673 \cdot 10^{-8}\,\Omega\,\mathrm{m}$	$2.655 \cdot 10^{-8}\,\Omega\,\mathrm{m}$
Densitiy	$7750\,\mathrm{kg/m^3}$	$8960\,\mathrm{kg/m^3}$	$2699\,\mathrm{kg/m^3}$
Temperature Coefficient α_t	$4 \cdot 10^{-3}/\mathrm{K}$	$3.93 \cdot 10^{-3}/\mathrm{K}$	-

Table 3.1: Material properties.

3.2 Accounting for temperature change

The rotor temperature varies significantly during one period of operation and one day of operation cycle (considering a typical day in a clinic). As a coupled thermal-magnetic model goes beyond the scope of this study, the temperature dependency of the material and the output respectively is accounted for by simulating every case for two temperatures, ”room” and ”operating” temperature. For better clarity, in each plot (in Chapter 4) the blue line stands for ”room temperature” (RT) and the red line stands for ”operating temperature” (OT) unless marked otherwise. Room temperature is assumed to be 20 °C for both, stator and rotor. The exemplary operating temperature is 400 °C for the rotor and 60 °C for the stator windings. The stator steel sheet is assumed to remain at ”room temperature” due to sufficient cooling by the surrounding cooling oil. [14]
To depict these temperature changes, the electric resistivity ρ was adjusted from its value at 20 °C to its particular temperature dependent value (3.1).

$$\rho = \rho_{20} \cdot [1 + \alpha_t \cdot \Delta T] \tag{3.1}$$

The exact temperature coefficient for the sheet metal in use is unknown leaving this value to a rough approximation, given by [31, p.435]. Therefore the quadratic temperature coefficient had to be disregarded leaving the obtained values to a rather rough estimation considering the non-linear behaviour of resistance change to temperature change. Yet again, to gain a general insight regarding the influence of temperature on the behaviour this approach is considered to be feasible. The material temperature coefficients are given in Table 3.1 and corresponding calculated parameters affected by temperature change are given in Table 3.2. Original values can be found in Table 2.2 and 3.1 respectively.

Parameter	Value
$\rho_{\mathrm{Cu},60\,^\circ\mathrm{C}}$	$1.94 \cdot 10^{-8}\,\Omega\,\mathrm{m}$
$\rho_{\mathrm{SM},400\,^\circ\mathrm{C}}$	$8.064 \cdot 10^{-7}\,\Omega\,\mathrm{m}$
$R_{\mathrm{S},60\,^\circ\mathrm{C}}$	$8.22\,\Omega$

Table 3.2: Parameter changed in JMAG.

3.3 Power and loss calculation

For ease of comparison, all losses are obtained at the operating point of 1 Nm. To validate the results all simulation results are compared to results obtained by analytical methods. To be able to present a clearly structured result chapter (4), the analytically obtained values are shown for the IM only.

Copper Losses

Copper losses in the stator windings are analytically accounted for by (3.2) [18] with the rms current value taken from FEA.

$$P_{\mathrm{Cu,Stator,total}} = I^2_{\mathrm{u,rms}} R_{\mathrm{S}} + I^2_{\mathrm{v,rms}} R_{\mathrm{S}} + I^2_{\mathrm{w,rms}} R_{\mathrm{S}} \tag{3.2}$$

Copper losses in the conductive layer of the IM rotor are roughly estimated with (3.3). At the average radius of the copper ring, the peak value of the axial component of the fundamental current density wave obtained with FEA was used. Sinusoidal distributed current density and no current density variation in radial direction was assumed. These results are compared with the results directly obtained with FEA.

$$P_{\mathrm{Cu,Rotor,layer}} = \int_V J^2 \rho \, dV \tag{3.3}$$

Iron Losses

All iron losses are directly obtained with FEA. Note that stator iron losses are accounted for in post processing due to their insignificant influence on the output torque, and in the interest of simulation time reduction.

Electrical Power Calculation

To calculate the total electric power in the circuit, the voltage and current values obtained by FEA and (3.4) are used.

$$P_{\mathrm{el,avg}} = \overline{u_{\mathrm{u}}(t)\, i_{\mathrm{u}}(t) + u_{\mathrm{v}}(t)\, i_{\mathrm{v}}(t) + u_{\mathrm{w}}(t)\, i_{\mathrm{w}}(t)} \tag{3.4}$$

The same approach is implemented in the FEA calculation program. Considering that the induced voltages are obtained by the difference quotient between two samples, the actual value is in between these two obtained values. To satisfy the law of conservation of energy, a correction of the total electric power obtained by FEA is needed by calculating the average of two neighbouring points:

$$u_{\mathrm{corr}}(t) = \frac{u(t - \Delta t) + u(t)}{2}$$

with the sampling interval Δt.

Mechanical Power Calculation

Mechanical power can be simply calculated using the averaged torque obtained by FEA, the rotational speed of the rotor and (3.5).

$$P_{\mathrm{mech}} = \frac{2\pi n\, T_{\mathrm{avg}}}{60} \tag{3.5}$$

3.4 DQZ Transformation

To simplify analysis all values obtained for the SRMs are transformed to the well-known rotating reference frame. This transformation combines the three (inter-)dependent phase quantities down to two independent, orthogonal components. To conduct the transformation all values are multiplied with the transformation matrix M (3.6). The matrix basically combines Clarke and Park transform. θ represents the angular difference between two reference frames. To give an example the transformation is given for the time depended current vector (3.7) and its visualisation is shown in Fig. 1.3. [17, p. 997]

$$M = \begin{bmatrix} cos(\theta) & cos(\theta - \frac{2pi}{3}) & cos(\theta - \frac{4pi}{3}) \\ -sin(\theta) & -sin(\theta - \frac{2pi}{3}) & -sin(\theta - \frac{4\pi}{3}) \end{bmatrix} \tag{3.6}$$

$$\begin{bmatrix} I_\mathrm{d} \\ I_\mathrm{q} \end{bmatrix} = M \cdot \begin{bmatrix} i_\mathrm{u}(t) \\ i_\mathrm{v}(t) \\ i_\mathrm{v}(t) \end{bmatrix} \tag{3.7}$$

3.5 Approach to find operating point

For the two different types of drives, two different approaches were used to obtain the operating point of 1 Nm.

Induction Motor

The starting point for both drives is a constant voltage supply of $\bar{U}_\mathrm{ph} = 400\,\mathrm{V_{ac}}$ as this is the voltage supply for the original IM. It is assumed that, despite the slip, the rotational speed of the anode reaches a minimum speed of 10 800 rpm. Consequently the supply frequency for the operating point of 1 Nm was increased incrementally starting at 185 Hz. After finding the operating frequency, the corresponding speed-torque curve for this frequency (for a fixed voltage supply) was calculated. For the operating temperature, the supply frequency and slip had to be adjusted accordingly.

Synchronous Reluctance Motors

The torque of the SRM is studied as a function of current phase angle β in order to illustrate the phase angle dependency on the torque output, as shown in (1.6), and to obtain the most favourable current phase angle for each rotor at both operating temperatures (under the condition of maximum torque output). Firstly, all SRMs were supplied with the same voltage as the reference IM (400 V). Secondly, to keep copper losses low, the supply voltage amplitude height was adjusted to shift the peak of the obtained curve to 1 Nm. This approach is referred to as maximum torque control (MTC) or maximum torque per ampere (MTPA) as opposed to maximum power factor control (MPFC) or various other control strategies [32].

4 Results

4.1 Induction Motor

General Characteristic

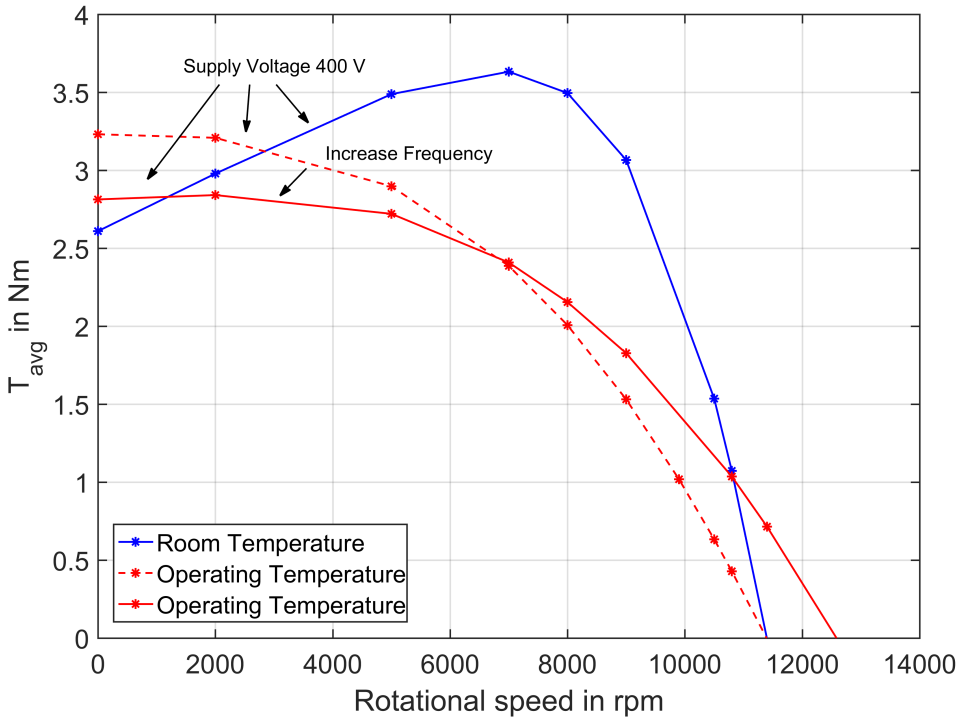

Fig. 4.1: Speed-Torque curve for both investigated temperatures and increased supply frequency for operating temperature.

	FEA		Calculated	
Parameter	Room T.	Operating T.	Room T.	Operating T.
T_{avg}	1.07 Nm	1.04 Nm	-	-
$I_{ph,rms}$	15.6 A	13.5 A	-	-
$P_{el,avg}$	6629 W	6020 W	6630 W	6021 W
P_{mech}	-	-	1210 W	1176 W
n_s	11 400 rpm	12 600 rpm	-	-
n	10 800 rpm	10 800 rpm	-	-
s	-	-	5.26 %	14.29 %

Table 4.1: Induction Motor Characteristics at investigated temperatures and the operation point.

The speed-torque curve for the IM at room temperature was obtained at 190 Hz. For the operating temperature, a higher frequency of 210 Hz had to be applied to reach the operating point of 1 Nm. This accompanies an increased slip from around 5 % to 14 % and can be explained by the increase of the rotor resistance (Fig. 4.1).

Where possible, all obtained FEA-values were validated with analytical estimation methods using FEA raw-data as described in the previous chapter. All acquired data, including a comparison of FEA and calculated values, is given in Table 4.1.

Another comparison between FEA and analytical methods was made regarding the total electric power in the circuit. Fig. 4.2a shows the total electric power as it was obtained with FEA. These values are compared to the value calculated with (3.4). Its corresponding curves are shown in Fig. 4.2b and exact values can be found in Table 4.1. Values show good agreement. The adjusted calculation method of $P_{el,avg}$ as described in Section 3.3 is considered and given in Section 4.1.

Torque over time is shown in Fig. 4.3 to give an idea of torque ripple.

To provide insight into the magnetic flux density distribution, Fig. 4.4 and Fig. 4.5 show the magnetic flux lines and the magnetic flux density at the operating point of 1 Nm and operating temperature.

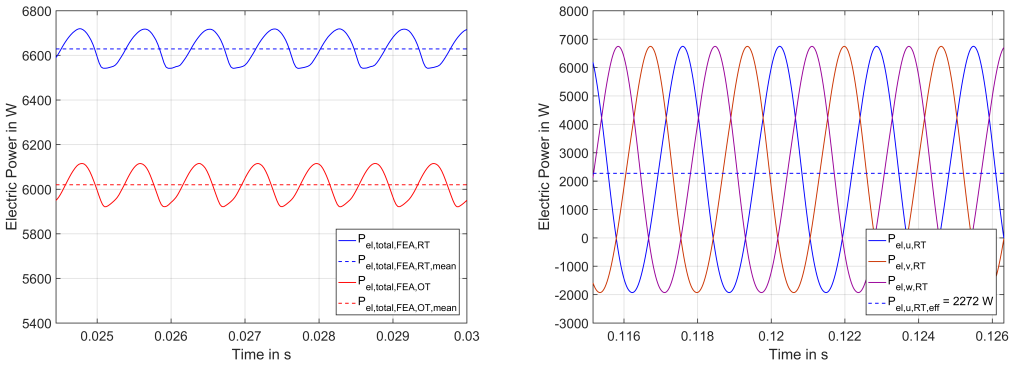

(a) (b)

Fig. 4.2: Circuit power comparison. Total electric power $P_{\mathrm{el,avg}}$ for both investigated temperatures is shown (a) and as an example the average value of the u-phase electric power obtained by analytical methods (3.4) for room temperature is given in (b) including the instantaneous power of all phases.

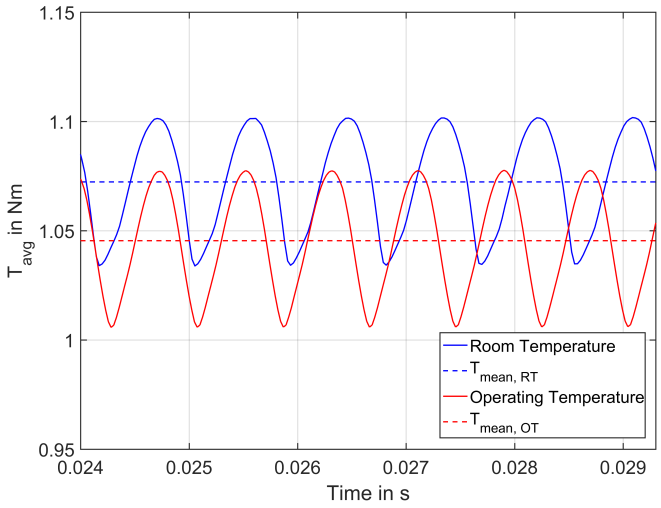

Fig. 4.3: Torque over time for both investigated temperatures for one mechanical revolution.

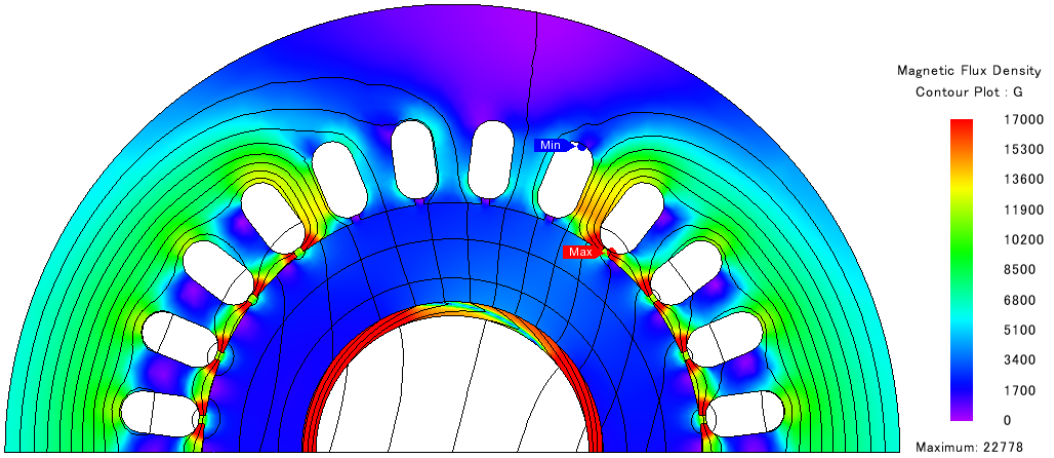

Fig. 4.4: Magnetic flux lines and contour plot of magnetic flux density in stationary mode at operating temperature and operation point.

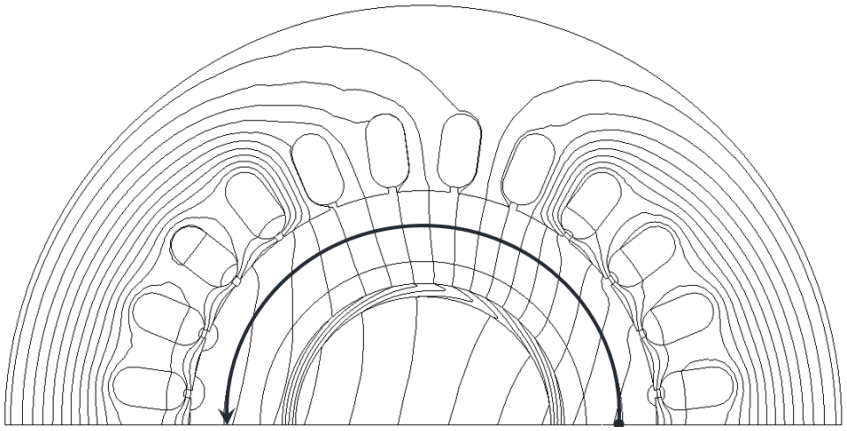

Fig. 4.5: Magnetic flux lines in stationary mode at operating temperature and operation point. The arrow marks the path along which the absolute value of the air gap flux density was obtained for (Fig. 4.6).

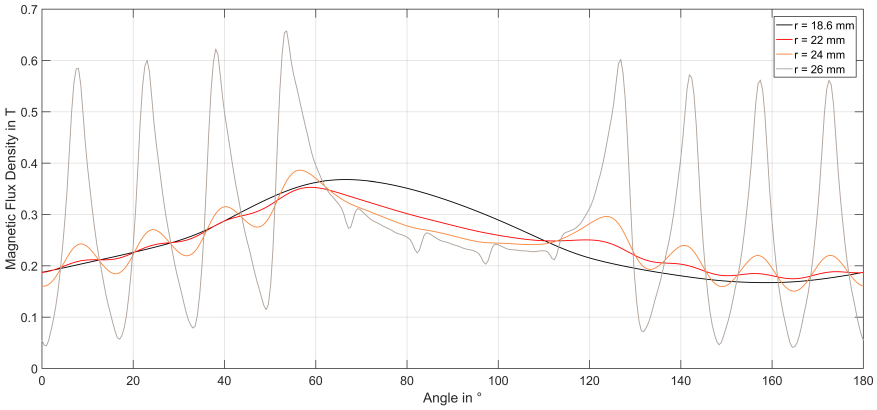

Fig. 4.6: Magnetic flux absolute value for four declining radii.

Fig. 4.6 reveals the behaviour of the magnetic field distribution along the air gap. Each line was obtained by starting at the anti-periodic boundary going in a half circle around the rotor with a certain radius (see Fig. 4.5). It can clearly be seen that with declining radius the harmonics caused by the stator slot openings smooth out. Underlining the possibility of a slot opening increase for higher flux yield.

Losses and energy balance

	FEA		Calculated	
Parameter	Room T.	Operating T.	Room T.	Operating T.
$P_{\text{Cu,Stator,total}}$	5158 W	4477 W	5161 W	4479 W
$P_{\text{Cu,Rotor,layer}}$	73 W	201 W	72 W	196 W

Table 4.2: IM loss comparison to calculated values ((3.2) and (3.3)).

A comparison of calculated values ((3.2) and (3.3)) and average values obtained by FEA are given in Table 4.2 and show good agreement. Subtracting all losses generated during the simulation from the total electric power leaves an unexplained mismatch of 186 W and 163 W for room and operating temperature respectively. Correcting the total electric power in the circuit with the method described in Section 3.3 gives adequate results leaving a difference of less than 0.1 % (see Table 4.3).

	Room T-		Operating T	
Parameter	FEA	Corrected FEA	FEA	Corrected FEA
$P_{\text{el,avg}}$	6629 W	6442 W	6020 W	5860 W
P_{mech}	- 1210 W	- 1210 W	- 1176 W	- 1176 W
$P_{\text{Cu,Stator,total}}$	- 5158 W	- 5158 W	- 4477 W	- 4477 W
$P_{\text{Cu,Rotor,layer}}$	- 73 W	- 73 W	- 201 W	- 201 W
$P_{\text{Fe,Rotor}}$	- 1 W	- 1 W	- 3 W	- 3 W
Mismatch	= 186 W	= - 1 W	= 163 W	= 4 W

Table 4.3: Induction Motor energy balance. Corrected FEA refers to Section 3.3.

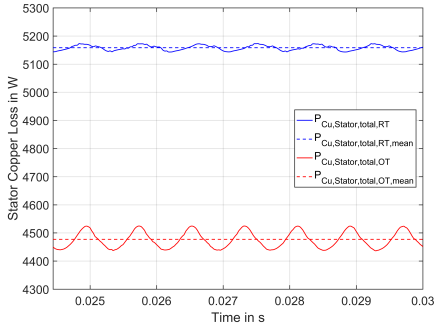

(a) Total stator copper losses.

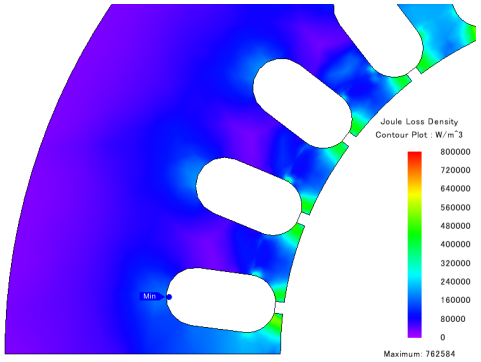

(b) Eddy current density expressed as joule loss density for all frequencies.

Fig. 4.7: Stator losses obtained by FEA.

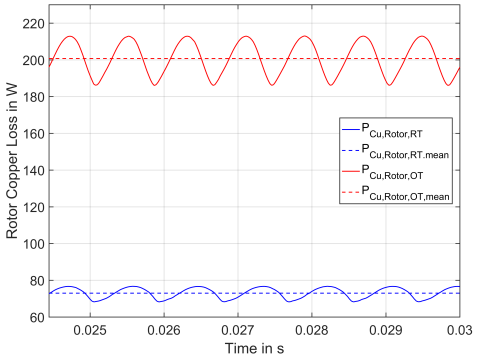

(a) Total rotor copper losses

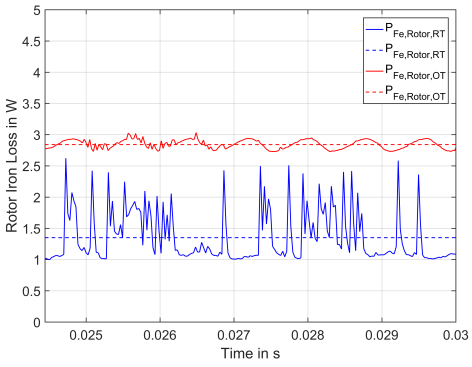

(b) Total rotor iron losses

Fig. 4.8: Rotor losses obtained by FEA.

4.2 Axially-layered Rotor

General Characteristics

Parameter	Room Temperature	Operating Temperature
$\bar{U}_{\mathrm{ph}}$	300 V	305 V
$I_{\mathrm{ph,rms}}$	9.4 A	8.7 A
T_{avg}	1.02 Nm	1 Nm
$P_{\mathrm{el,avg}}$	3047 W	3037 W
P_{mech}	1154 W	1131 W
$\beta_{\mathrm{T_{max}}}$	60.3°	52.2°
L_{d}	0.0241 H	0.0241 H
L_{q}	0.0149 H	0.0149 H
ξ	1.616	1.614
ζ	0.0092	0.0091
$PF_{\phi_{\mathrm{s}}}$	0.504	0.533

Table 4.4: Characteristics of axially-layered rotor at investigated temperatures and operating point of 1 Nm.

Table 4.4 gives an overview of the characteristics of the axially-layered rotor at the investigated temperatures.

The torque dependency on the current phase angle β is shown in Fig. 4.9. The upper curves were obtained by keeping the same supply voltage of 400 V as applied to the reference induction motor. For the lower curves, the supply voltage was adjusted to shift the highest average torque to 1 Nm. The dashed lines indicate a current phase angle shift to lower values when reducing the supply voltage with fixed angle between supply voltage, state space phasor, and rotor d-axis (refers to angle α in Fig. 1.3). Considering that the stator iron losses (refers to resistance R_{m1} in the circuit diagrams, Fig. 1.2) are neglected, the highest average torque is expected to occur at $\beta = 45°$. However, due to the applied voltage-control, the phase current I_{ph} and consequently I_{d} and I_{q} are not fixed and establish themselves 4.19.

Note that it can be assumed that the curves with reduced supply voltage would perfectly overlap if more values between $\beta = 50°$- $60°$ had been

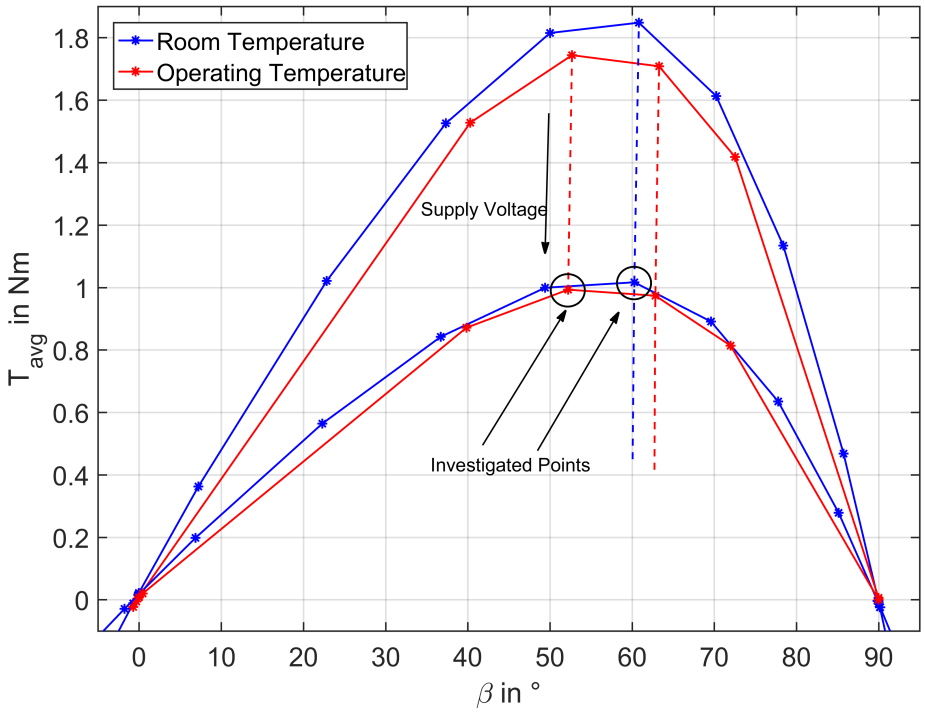

Fig. 4.9: Variation of torque with respect to the variation of β for two temperatures and reduced supply voltages

investigated since a change of magnetic characteristics with increasing temperature was not taken into account.

Fig. 4.10 shows a decrease of the magnetizing inductance L_d when I_d is increased (due to increasing supply voltage) and I_q equals zero (and vice versa for L_q and I_q). I_q is much higher than I_d most likely explaining the bigger gradient of L_q when compared to L_d. For a deeper insight into the behaviour of L_d and L_q, more current values would have to be investigated. Though the values of L_d and L_q decrease as the current is increased, the saliency ratio ξ increases (Fig. 4.11). In the case of operating temperature ξ is higher than in the case of room temperature. Note again that to obtain the points in Fig. 4.10 and Fig. 4.11, the supply voltage was fixed to the given value. Consequently L_d and L_q are calculated at different current values.

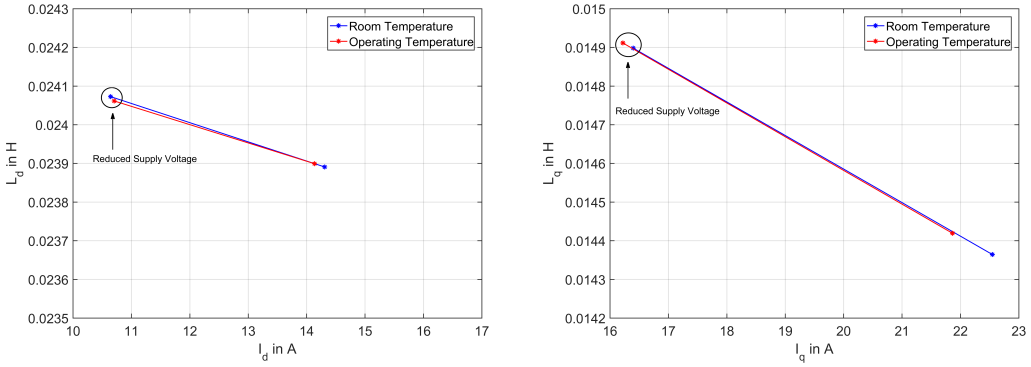

Fig. 4.10: L_d and L_q inductances for both investigated temperatures for $\beta \approx 0°$, $I_\mathrm{q} \approx 0\,\mathrm{A}$ (a) and $\beta \approx 90°$, $I_\mathrm{d} \approx 0\,\mathrm{A}$ (b). Starting with the supply voltage of 400 V reducing it to the operating points 300 V for room temperature and 305 V for operating temperature. Using the same relative scale exaggerated decrease of L_q inductance becomes obvious.

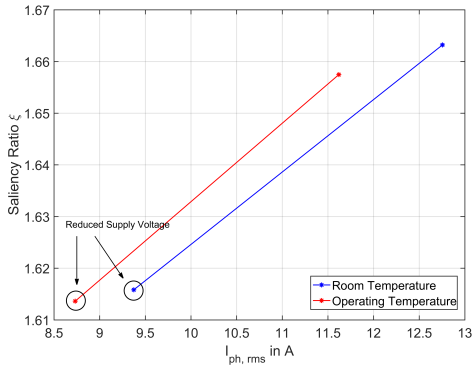

Fig. 4.11: Influence of temperature and phase current on saliency ratio.

Therefore ξ refers to the saliency ratio for the given and fixed supply voltage. However, depending on the saturation state of the rotor, current control (calculating L_d and L_q from values when only d- or q-axis excitation is applied, but with the same current value) is expected to deliver different saliency ratios. The values of L_d and L_q can be obtained when β is 0° and 90° respectively. This is equal to a torque output of zero. Subsequently α was varied until a torque output of zero was obtained from FEA.

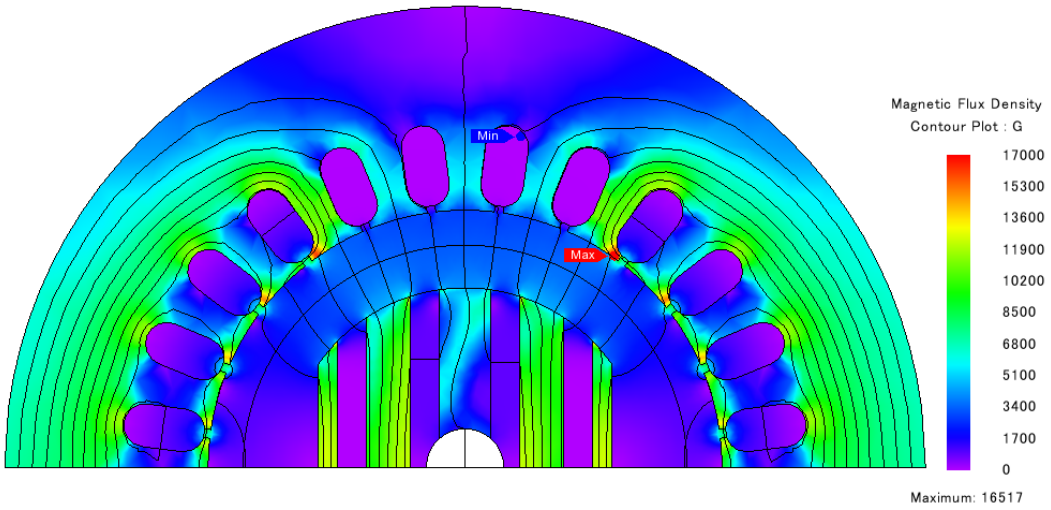

Fig. 4.12: Magnetic flux lines and magnetic flux density contour plot
$\beta \approx 0°$, $I_q \approx 0\,A$

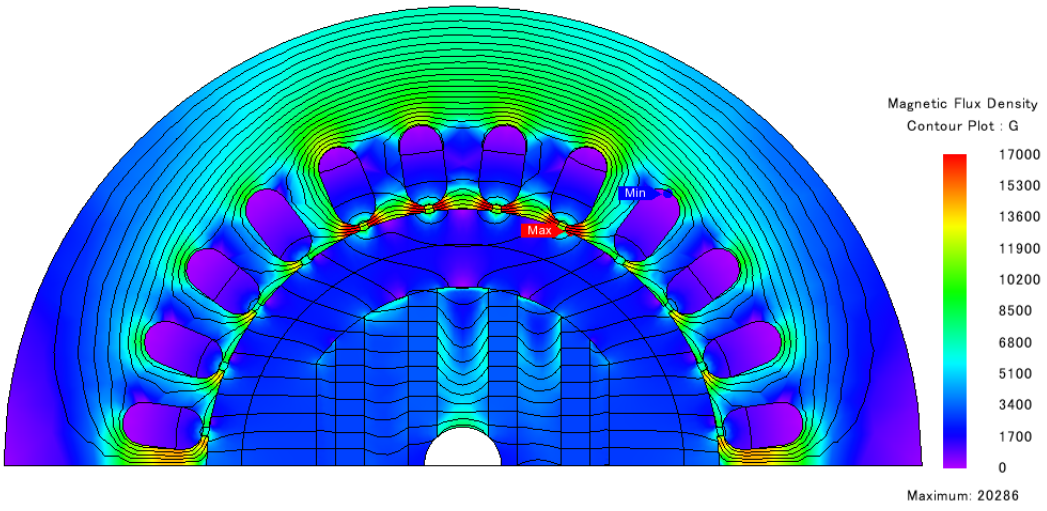

Fig. 4.13: Magnetic flux lines and magnetic flux density contour plot
$\beta \approx 90°$, $I_d \approx 0\,A$

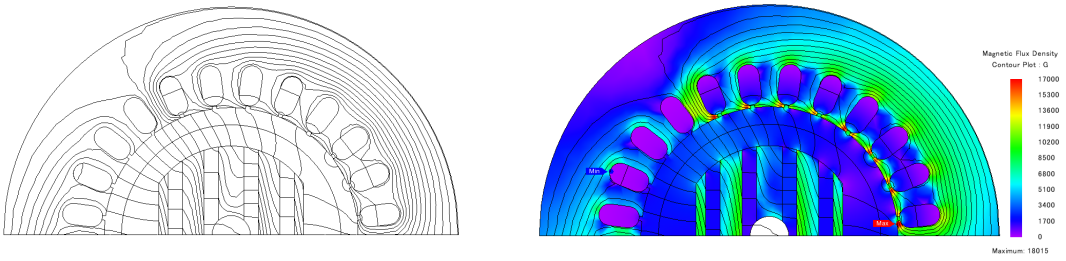

(a) (b)

Fig. 4.14: Magnetic flux lines/density for maximum torque at operating temperature.

Fig. 4.12 and Fig. 4.13 show the magnetic flux distribution for $\beta \approx 0°$ and $\beta \approx 90°$ respectively. The difference in the magnetic flux distribution of just d-axis or just q-axis excitation can clearly be seen. In Fig. 4.12 all flux lines in the rotor are located within the magnetic material of the rotor whereas in the case of q-axis excitation (Fig. 4.13) all magnetic flux lines have to pass through the non-magnetic material as well. This explains why I_q in the case of $I_d \approx 0\,A$ (Fig. 4.10b) is much higher than in the opposite case (Fig. 4.10a). To emphasise the difference of the magnetic flux distribution in the case of maximum torque output, the magnetic flux lines and the corresponding contour plot is shown (Fig. 4.14). The contour plot reveals saturated parts in the stator teeth at the stator slot openings.

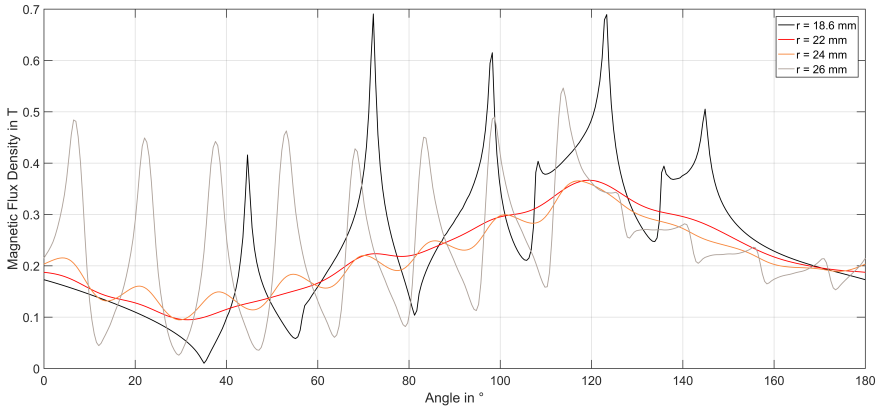

Fig. 4.15: Magnetic flux absolute value for four declining radii obtained by the simulation showed in Fig.4.14.

Fig. 4.15 reveals the behaviour of the magnetic field distribution along the air gap. Each line was obtain by starting at the anti-periodic boundary going in a half circle around the rotor with a certain radius (see Fig. 4.6). It can clearly be seen that with the declining radius, the harmonics caused by the stator slot openings smooth out (radius 22 mm and 24 mm). Moving closer towards the rotor, the five magnetic layers become more prominent as most of the flux lines pass through these layers causing the magnetic flux distribution to loose its smoothed out shape.

To verify the accuracy of the calculated inductances L_d and L_q and values for β, a comparison between the torque values calculated with (1.5) and (1.6) and the torque output for every value of β at the same time step obtained by FEA is made in Fig. 4.16a. In Fig. 4.16b a comparison of the torque output over time for the two operation points is shown. These values are also calculated with the same formulas. Both figures show values for room temperature and reduced voltage. The obtained values show good congruence. This proves that for this specific rotor, the saturation state and consequently neither the calculated saliency ratio nor the torque index vary significantly with β and current.

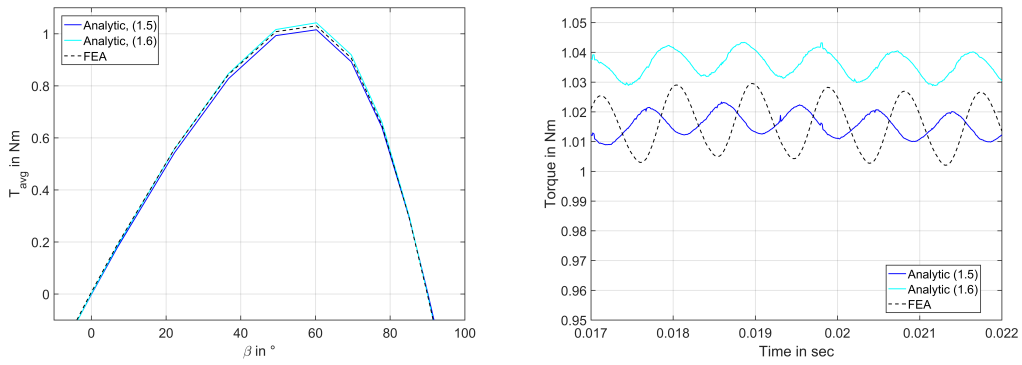

(a) (b)

Fig. 4.16: Proving the accuracy of the calculated values β, L_d and L_q. Comparison of torque over beta (a) and torque over time (b) obtained by FEA with calculated torque using (1.5) and (1.6). All values refer to room temperature.

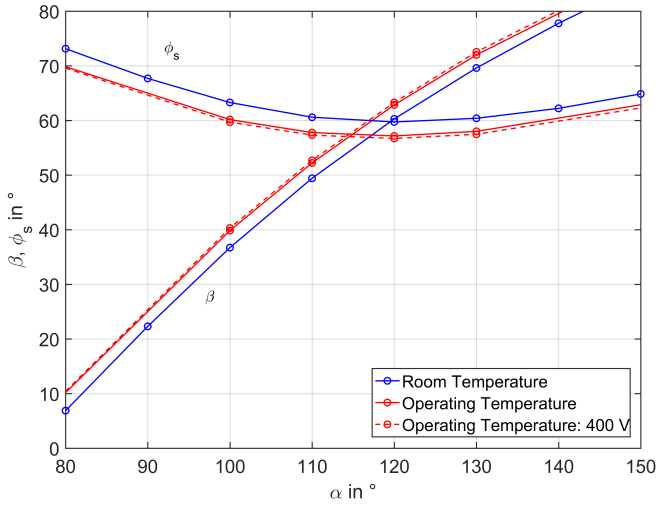

Fig. 4.17: Non-linear behaviour of β and ϕ_s when rotating the U-phasor (corresponds to increasing α).

Fig. 4.17 shows the values for β and ϕ_s with respect to α, which represents the angle between the U-phasor and the d-axis. This angle is formed by the sum of β and ϕ_s. Consequently ϕ_s was calculated by subtracting β from α. It shows the non-linear behaviour of β and ϕ_s when increasing α. This refers to a rotation of the stator voltage state phasor. An additional dashed line represents the same values for the original supply voltage of 400 V at operating temperature. By comparing the dashed red line with the solid red line it can be stated that the value of the supply voltage does not influence the phasor diagram significantly.

The influence of the stator winding resistance R_s on the power factor becomes obvious when looking at Fig. 4.18. It shows the power factor obtained neglecting (dashed lines) and including (solid lines) R_s for every simulated value of β and both investigated temperatures. Looking at the solid blue lines (representing room temperature) it seems that for both control strategies (MTC and MPFC) β is the same. This is in contrast to the operating temperature where it appears that β should be shifted to higher values to obtain maximum power factor. As the simulation was carried out with voltage-control, the phase current for every β was calculated. A current-controlled

drive will be left for further investigation (Fig. 4.19). A few additional simulation results for all three rotors are shown in Appendix A.

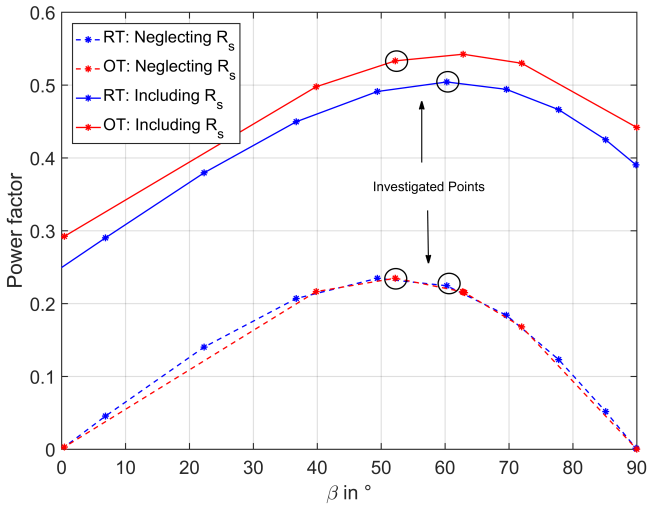

Fig. 4.18: Calculated power factor for various β with two analytical equations (1.11) and (1.9) showing the influence of R_s on the power factor.

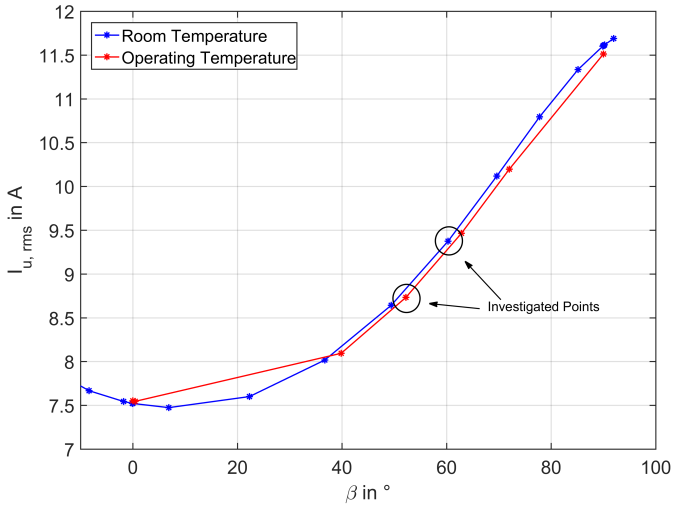

Fig. 4.19: Phase current $I_{u,rms}$ for various β and constant supply voltage.

Energy Balance

	Room T		Operating T	
Parameter	FEA	Corrected FEA	FEA	Corrected FEA
$P_{\text{el,total}}$	3047 W	3025 W	3037 W	3016 W
P_{mech}	- 1154 W	- 1154 W	- 1131 W	- 1131 W
$P_{\text{Cu,Stator,total}}$	- 1877 W	- 1877 W	- 1888 W	- 1888 W
$P_{\text{Fe,Rotor}}$	- 0 W	- 0 W	- 0 W	- 0 W
Mismatch	= 16 W	= - 6 W	= 18 W	= - 3 W

Table 4.5: Axially-layered rotor energy balance. Corrected FEA refers to Section 3.3

Table 4.5 sums all acquired losses (rounded to integer) during the simulation ($P_{\text{Fe,Rotor}}$ and $P_{\text{Cu,Stator,total}}$, also see Fig. 4.20). Correcting the obtained value $P_{\text{el,total}}$ leaves an acceptable mismatch of around 0.1 % - 0.2 %.

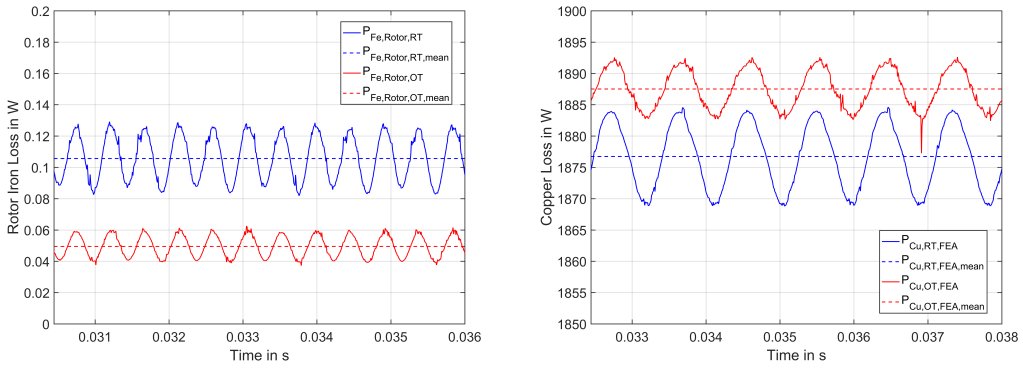

(a) (b)

Fig. 4.20: Losses acquired during simulation: $P_{\text{Fe,Rotor}}$ (a) and $P_{\text{Cu,Stator,total}}$ (b).

4.3 Solid Salient Rotor

Plots and investigated parameters coincide with the axially-layered rotor and a detailed description of the plots can be found in Section 4.2. Only the significant differences and unique characteristics are pointed out in the following two sections.

General Characteristics

Parameter	Room Temperature	Operating Temperature
$\bar{U}_{\mathrm{ph}}$	350 V	360 V
$I_{\mathrm{ph,rms}}$	10.3 A	10.5 A
T_{avg}	1 Nm	0.99 Nm
$P_{\mathrm{el,avg}}$	3427 W	3894 W
P_{mech}	1131 W	1120 W
$\beta_{\mathrm{T_{max}}}$	56.2°	58.9°
L_{d}	0.0218 H	0.0217 H
L_{q}	0.0168 H	0.0168 H
ξ	1.3	1.29
ζ	0.005	0.005
$PF_{\phi_{\mathrm{s}}}$	0.442	0.483

Table 4.6: Characteristics solid salient rotor at investigated temperatures and operating point of 1 Nm.

Table 4.6 gives an overview of the characteristics of the solid salient rotor at the investigated temperatures.

The torque dependency on the current phase angle β is shown in Fig. 4.21. The supply voltage for the operating temperature was increased again and for this rotor the phase currents $I_{\mathrm{ph,rms}}$ (10.3 A and 10.5 A for room and operating temperatures respectively) closely match, resulting in an almost exact overlay of both curves.

Fig. 4.22 shows a stronger decrease of the magnetizing inductance L_{d} when compared to L_{q}. However, the saliency ratio ξ increases (Fig. 4.23) with increasing phase current.

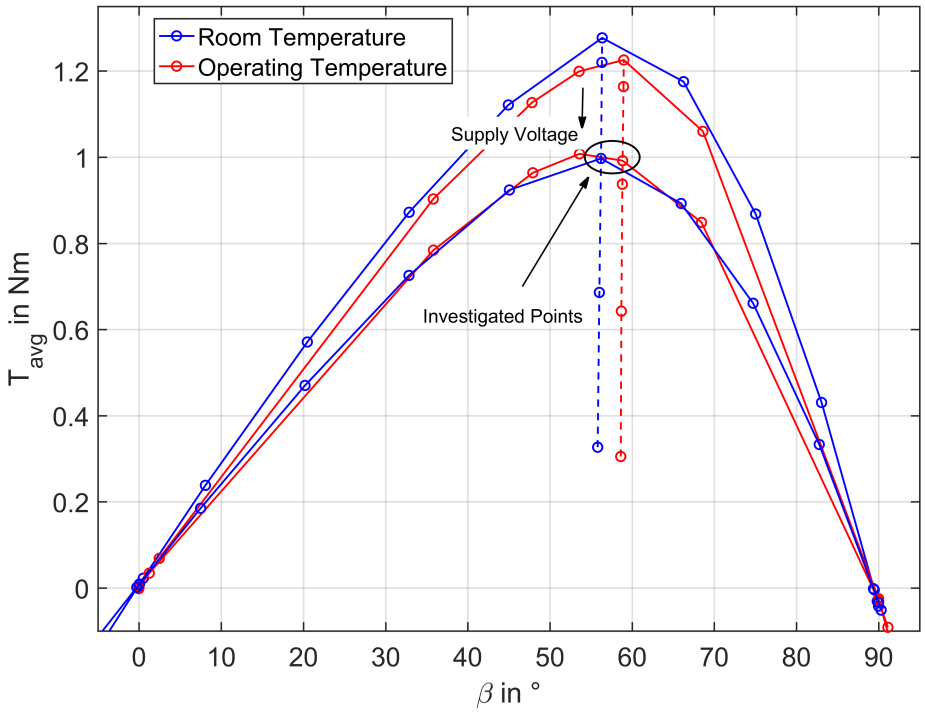

Fig. 4.21: Variation of torque with respect to the variation of β for two temperatures and reduced supply voltages

Fig. 4.24 and Fig. 4.25 reveal the magnetic flux distribution for $\beta \approx 0°$ and $\beta \approx 90°$ at reduced supply voltage and operating temperature respectively. As with the axially-layered rotor, the difference in the magnetic flux distribution of just d-axis or just q-axis excitation can clearly be seen. In Fig. 4.24 all flux lines contributing to the useful magnetic flux enter the rotor along the narrow side whereas in the case of q-axis excitation (Fig. 4.25), the magnetic flux path is much longer and distributed along the long side of the rotor.

Fig. 4.24 and the magnetic flux lines and density for maximum torque at operating temperature (Fig. 4.26) show a saturated part next to the rotor shaft which gives potential for optimization.

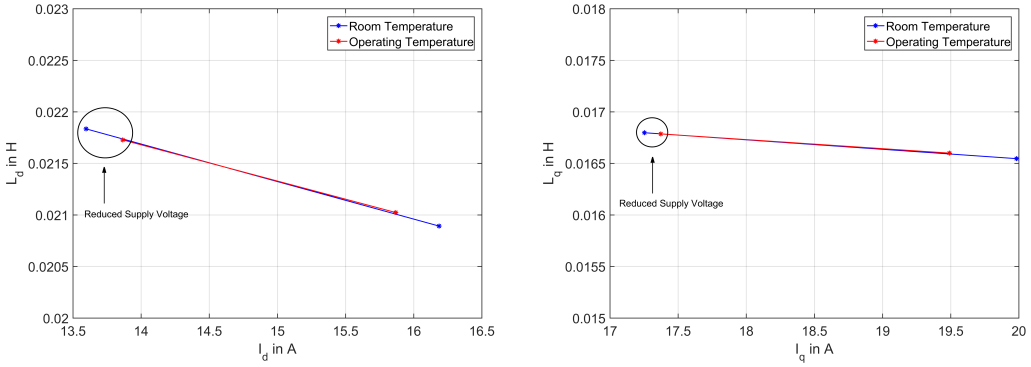

(a) (b)

Fig. 4.22: L_d and L_q inductances for both investigated temperatures for $\beta \approx 0°$, $I_q \approx 0\,A$ (a) and $\beta \approx 90°$, $I_d \approx 0\,A$ (b). Starting with the supply voltage of 400 V reducing it to the operating points 350 V for room temperature and 360 V for operating temperature. Using the same relative scale a stronger decrease of L_d inductance is obvious even at lower current values I_d .

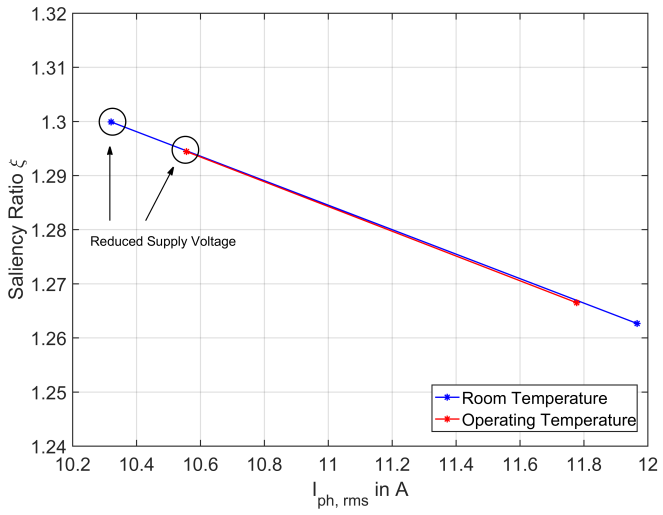

Fig. 4.23: Influence of temperature and phase current on saliency ratio.

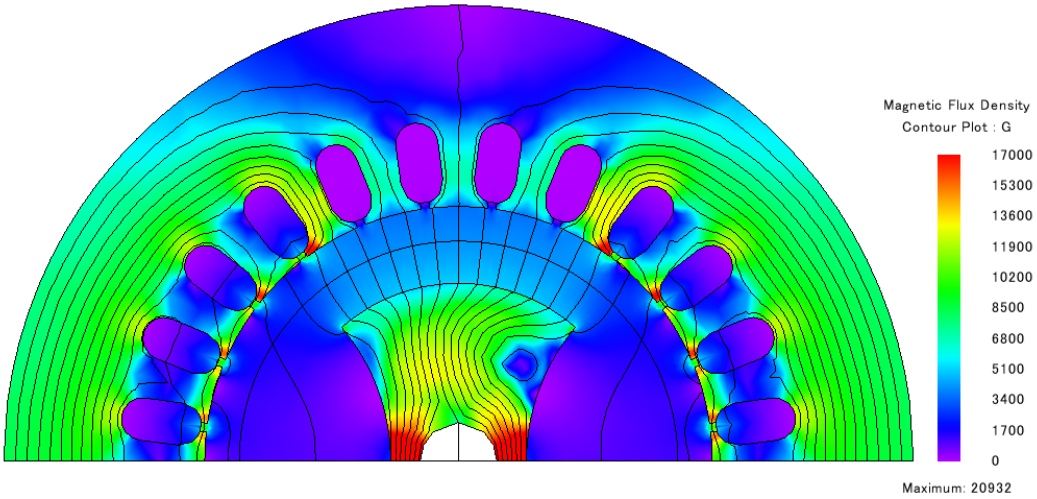

Fig. 4.24: Magnetic flux lines and magnetic flux density contour plot
$\beta \approx 0°$, $I_q \approx 0\,A$

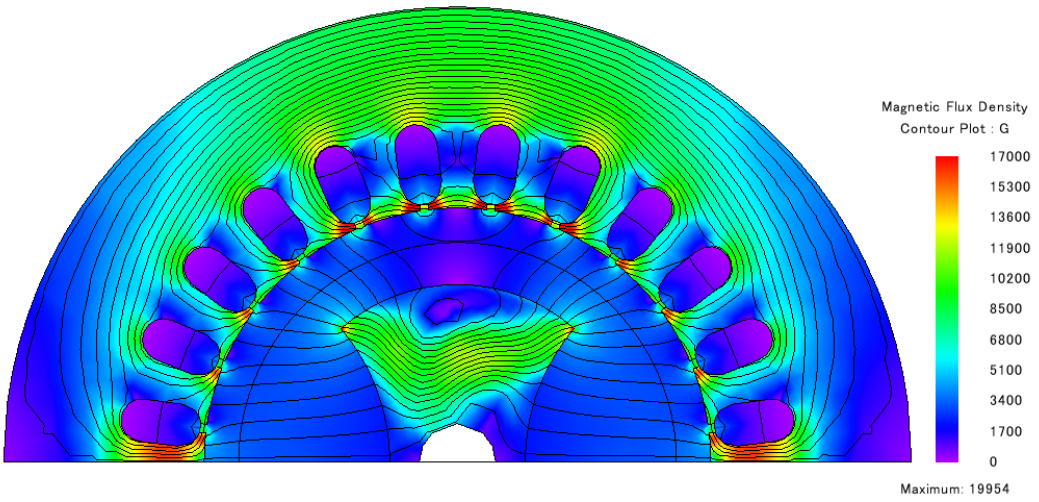

Fig. 4.25: Magnetic flux lines and magnetic flux density contour plot
$\beta \approx 90°$, $I_d \approx 0\,A$

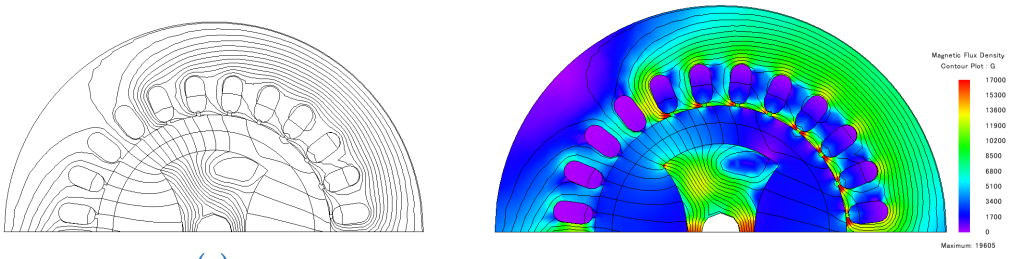

(a) (b)

Fig. 4.26: Magnetic flux lines/density for maximum torque at operating temperature.

The radial magnetic flux distribution along the air gap in Fig. 4.27 again shows the influence of the rotor shape. The highest peak at around 130° reflects the increased magnetic flux density at the left corner of the rotor.

Comparing torque values calculated with (1.5) and (1.6) with the torque output for every value of β at the same time step obtained by FEA (Fig. 4.28) reveals a discrepancy between T_{avg} calculated with (1.6) and T_{avg} obtained with the other two methods. This is due to the influence of saturation on the calculated inductances. By comparing the magnetic flux density plots for $\beta \approx 0°$ (Fig. 4.24) and $\beta_{T_{\text{max}}} \approx 60°$ (Fig. 4.26) it can clearly be seen that for maximum torque output the saturated parts in Fig. 4.24 show less magnetization leading to an increased magnetizing inductance L_{d}. This proposition can be justified by calculating the magnetizing inductances for decreased I_{d} and I_{q}.

Again it appears that for both control strategies (MTC and MPFC) the current angle β is almost the same (Fig. 4.29). Furthermore it is notable that the phase current starting from β =0° decreases until at around β =20° where $I_{\text{u,rms}}$ starts to increase (Fig. 4.40b). Again this can be reduced to the influence of saturation.

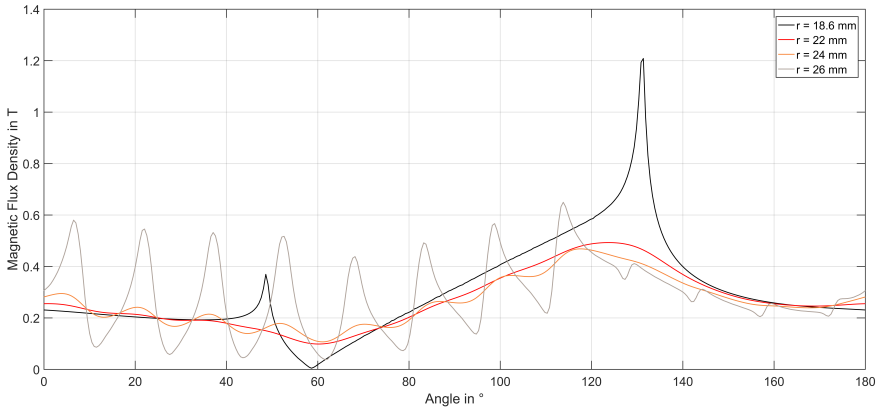

Fig. 4.27: Magnetic flux absolute value for four declining radii obtained by the simulation showed in Fig.4.26.

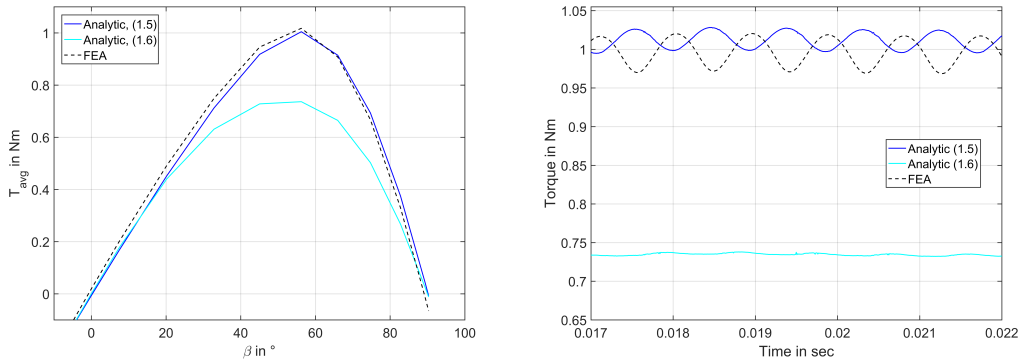

(a) (b)

Fig. 4.28: Comparison of torque over beta (a) and torque over time (b) obtained by FEA Simulation with calculated torque using (1.5) and (1.6). All values refer to room temperature.

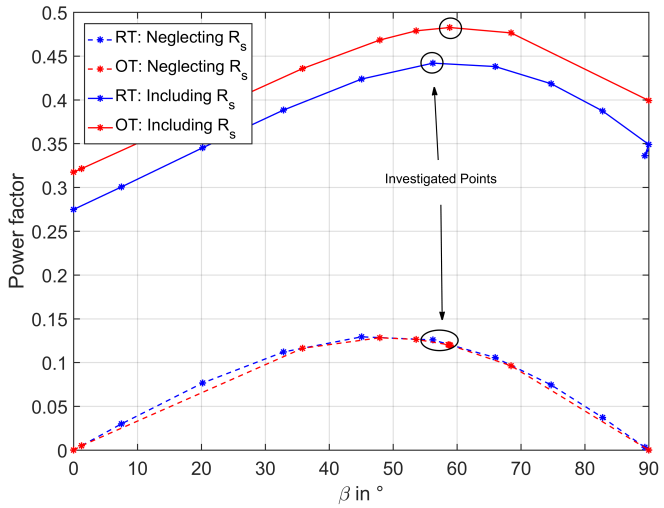

Fig. 4.29: Calculated power factor for various β including the influence of R_s in the calculation.

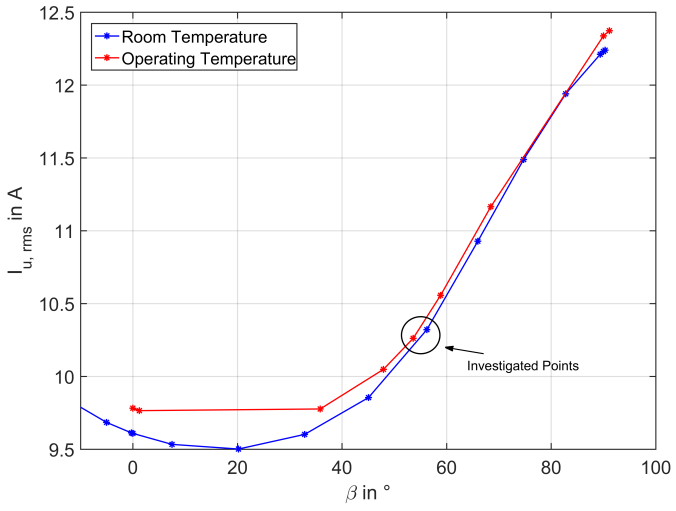

Fig. 4.30: Phase current $I_{u,rms}$ for various β and constant supply voltage.

Energy balance

	Room T		Operating T	
Parameter	FEA	Corrected FEA	FEA	Corrected FEA
$P_{\text{el,total}}$	3427 W	3397 W	3894 W	3863 W
P_{mech}	- 1131 W	- 1131 W	- 1120 W	- 1120 W
$P_{\text{Cu,Stator,total}}$	- 2272 W	- 2272 W	- 2739 W	- 2739 W
$P_{\text{Fe,Rotor}}$	- 0 W	- 0 W	- 0 W	- 0 W
Mismatch	= 24 W	= - 6 W	= 35 W	= 5 W

Table 4.7: Solid Salient rotor energy balance. Corrected FEA refers to Section 3.3

Table 4.7 sums all acquired losses (rounded to integer) during the simulation ($P_{\text{Fe,Rotor}}$ and $P_{\text{Cu,Stator,total}}$, also see Fig. 4.31) including the corrected value for $P_{\text{el,total}}$.

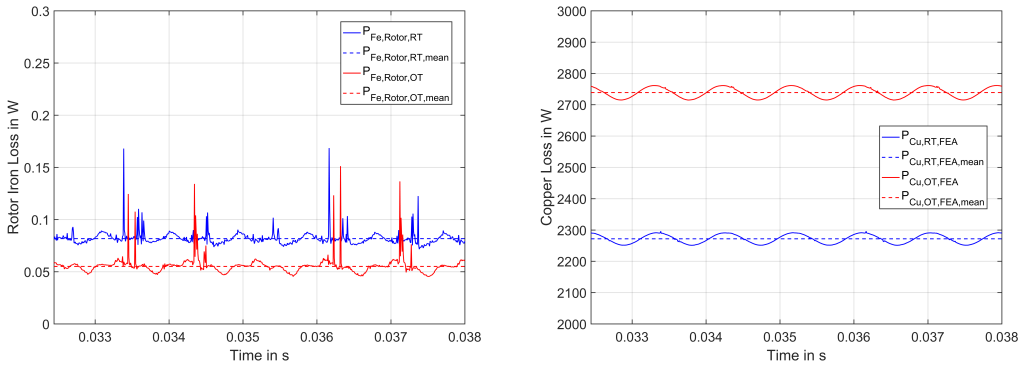

(a) (b)

Fig. 4.31: Losses acquired during simulation: $P_{\text{Fe,Rotor}}$ (a) and $P_{\text{Cu,Stator,total}}$ (b).

4.4 Ring Salient Rotor

General Characteristics

Parameter	Room Temperature	Operating Temperature
$\bar{U}_{ph}$	540 V	550 V
$I_{ph,rms}$	22 A	21 A
T_{avg}	0.99 Nm	1 Nm
$P_{el,avg}$	11 442 W	12 283 W
P_{mech}	1120 W	1131 W
$\beta_{T_{max}}$	126.97°	119.62°
L_d	0.0127 H	0.0129 H
L_q	0.014 H	0.0142 H
ξ	0.907	0.908
ζ	−0.0013	−0.0013
PF_{ϕ_s}	0.454	0.494

Table 4.8: Characteristics of ring salient rotor at investigated temperatures and operating point of 1 Nm.

Table 4.8 gives an overview of the characteristics of the ring salient rotor at the investigated temperatures.

The torque dependency on the current phase angle β is shown in Fig. 4.32. The supply voltage for both investigated temperatures was drastically increased and the phase currents $I_{ph,rms}$ (22 A and 21 A for room and operating temperatures respectively) are significantly higher than for the axially-layered and solid salient rotor shapes.

Unlike the solid salient rotor the ring salient rotor shows stronger decreasing L_q than L_d magnetizing inductance (Fig. 4.33). When looking at the contour plots (Fig. 4.35 and Fig. 4.36) this is most likely due to the fact that the rotor is already highly saturated in the case of just d-axis excitation and the increasing supply voltage does not lead to a higher magnetization of the rotor. L_d is smaller than L_q and consequently the saliency ratio of the rotor for fixed supply voltage is below zero (Fig. 4.34).

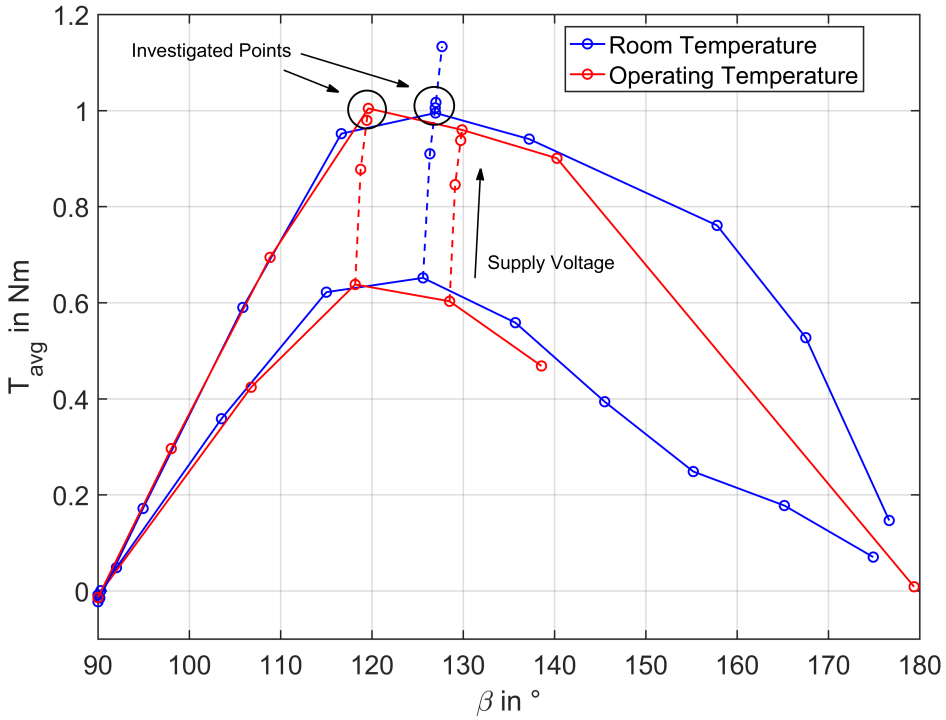

Fig. 4.32: Variation of torque with respect to the variation of β for two temperatures and increased supply voltages

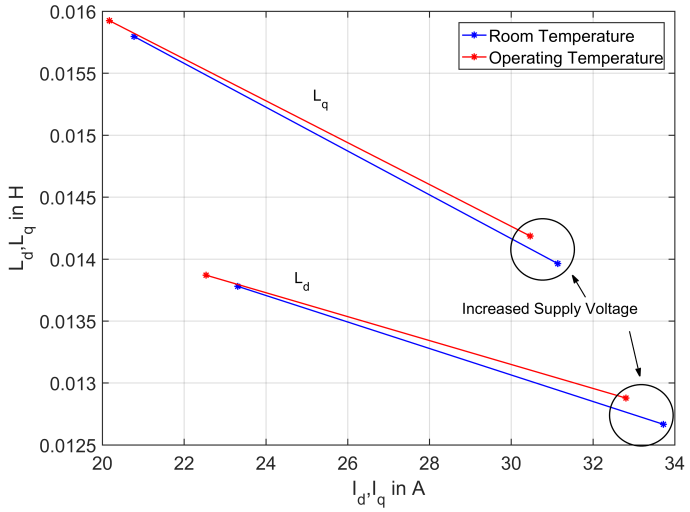

Fig. 4.33: L_d and L_q inductances for both investigated temperatures for $\beta \approx 0°$, $I_q \approx 0\,A$ and $\beta \approx 90°$, $I_d \approx 0\,A$. Starting with the supply voltage of 400 V increasing it to the operating points 540 V for room temperature and 550 V for operating temperature a stronger decrease of L_q inductance is obvious.

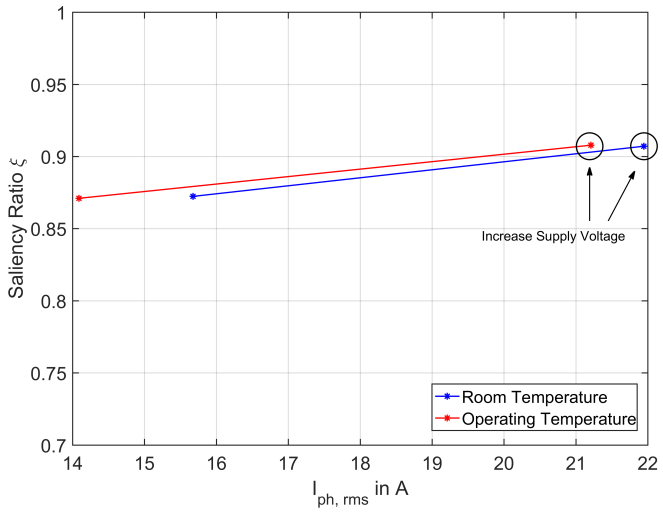

Fig. 4.34: Influence of temperature and phase current on saliency ratio.

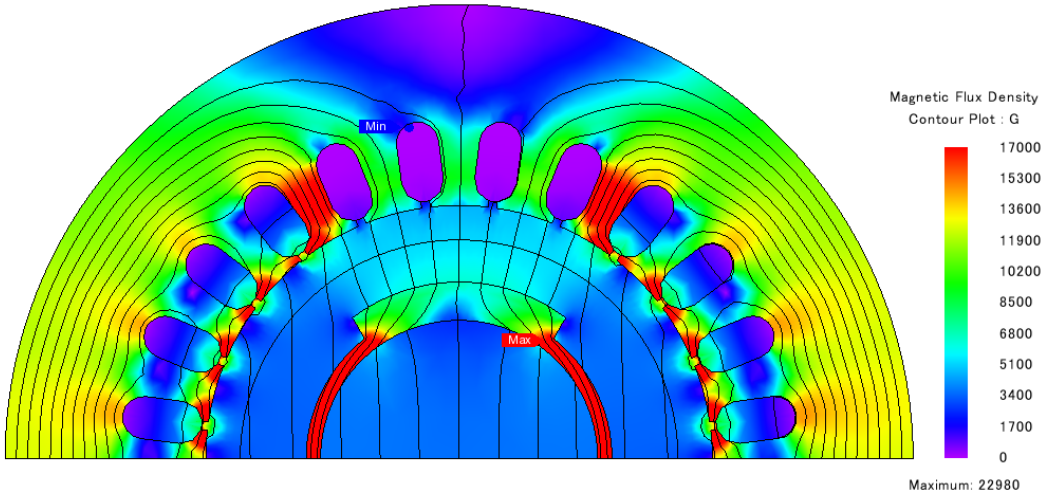

Fig. 4.35: Magnetic flux lines and magnetic flux density contour plot
$\beta \approx 0°$, $I_q \approx 0\,A$

Fig. 4.35 and Fig. 4.36 reveal the magnetic flux distribution for $\beta \approx 0°$ and $\beta \approx 90°$ respectively. The difference in the magnetic flux distribution of just d-axis or just q-axis excitation is not as obvious as with the axially-layered and solid salient rotor shapes since this rotor is highly saturated in both cases. However, it seems that in the case of just d-axis excitation, the magnetic reluctance is higher than in the opposite case explaining why the magnetizing inductance L_d is lower than the magnetizing inductance L_q. This reversal is also responsible for the rather unusual value of $\beta_{T_{max}}$. The corresponding magnetic flux lines and contour plot can be seen in Fig. 4.37

The radial magnetic flux distribution along the air gap in Fig. 4.38 again shows the influence of the rotor shape.

Comparing torque values calculated with (1.5) and (1.6) and the torque output for every value of β at the same time step obtained by FEA (Fig. 4.39) show a rather big discrepancy due the highly saturated rotor and stator parts.

Calculation of PF with (1.9) gives negative results because, as mentioned, the saliency ratio is below one (Fig. 4.40a). The calculated power factor

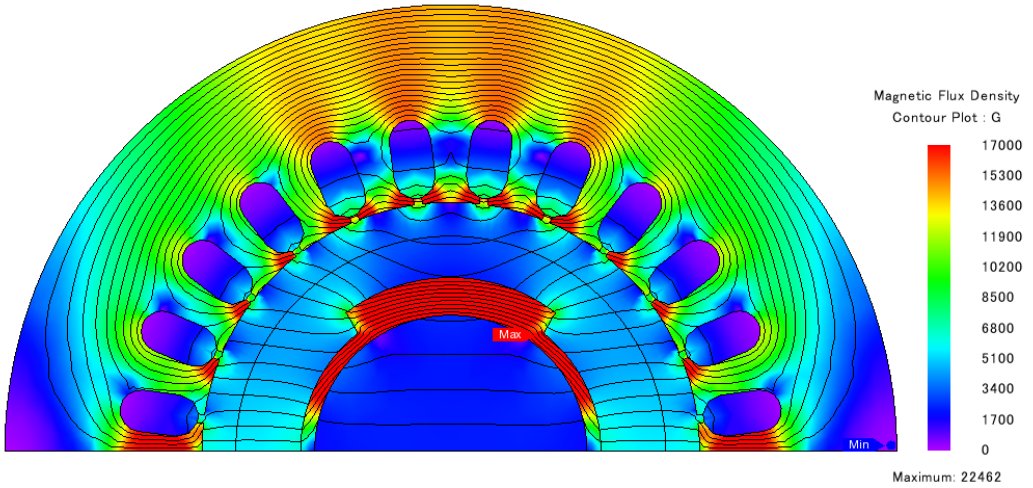

Fig. 4.36: Magnetic flux lines and magnetic flux density contour plot
$\beta \approx 90°$, $I_d \approx 0\,\mathrm{A}$

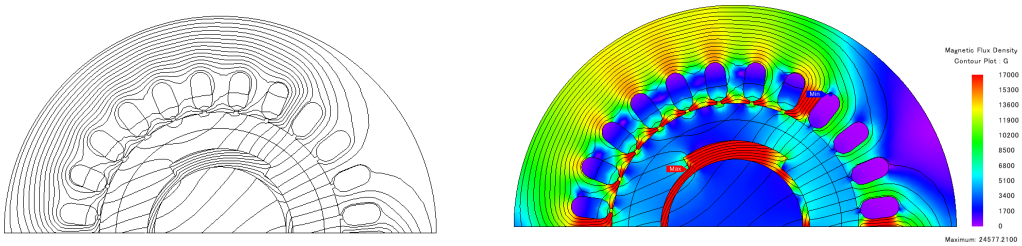

(a) (b)

Fig. 4.37: Magnetic flux lines/density for maximum torque at operating temperature.

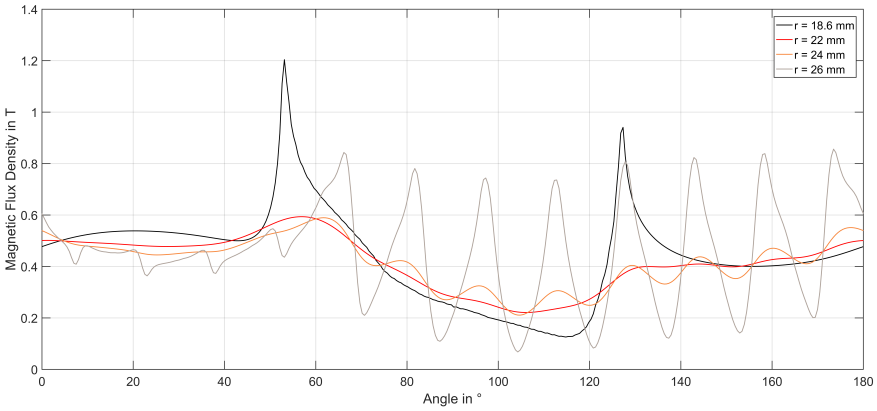

Fig. 4.38: Magnetic flux absolute value for four declining radii obtained by the simulation showed in Fig.4.37.

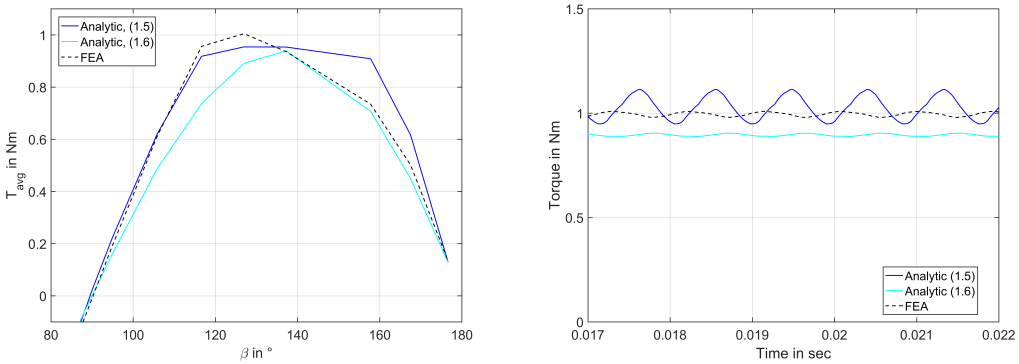

(a) (b)

Fig. 4.39: Comparison of torque over beta (a) and torque over time (b) obtained by FEA Simulation with calculated torque using (1.5) and (1.6). All values refer to room temperature.

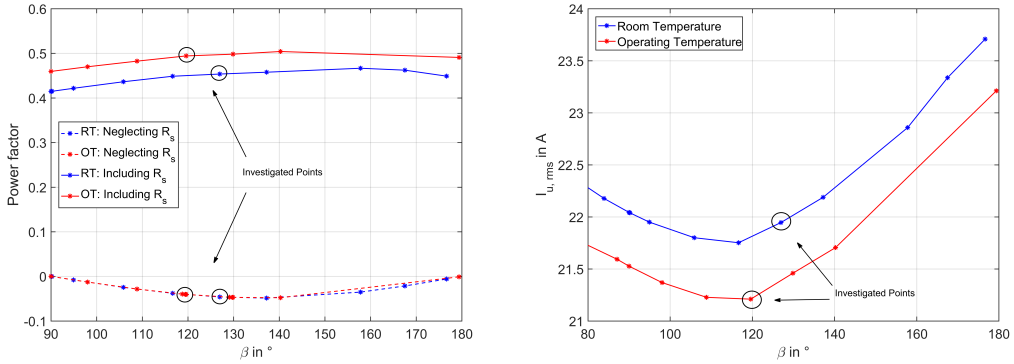

(a) (b)

Fig. 4.40: (a) Calculated power factor for various β. (b) Phase current $I_{\mathrm{u,rms}}$ for various β and constant supply voltage.

calculated with the actual phase shift between voltage and current (obtained with state phasor values) (1.11) considering R_{m1} gives accurate results.

As the simulation was carried out with voltage-control, the phase current for every β was calculated (Fig. 4.40b). It is notable that the phase current, starting from β =90°, decreases until around β =120° where $I_{\mathrm{u,rms}}$ starts to increase. This can again be reduced to the influence of saturation.

Energy balance

	Room T		Operating T	
Parameter	FEA	Corrected FEA	FEA	Corrected FEA
$P_{\text{el,total}}$	11 442 W	11 345 W	12 283 W	12 189 W
P_{mech}	- 1120 W	- 1120 W	- 1131 W	- 1131 W
$P_{\text{Cu,Stator,total}}$	- 10 217 W	- 10 217 W	- 11 052 W	- 11 052 W
$P_{\text{Fe,Rotor}}$	- 2 W	- 2 W	- 1 W	- 1 W
Mismatch	= 104 W	= 7 W	= 99 W	= 5 W

Table 4.9: Ring salient rotor energy balance. Corrected FEA refers to Section 3.3

Table 4.9 sums all acquired losses (rounded to integer) during the simulation ($P_{\text{Fe,Rotor}}$ and $P_{\text{Cu,Stator,total}}$) including the corrected value for $P_{\text{el,total}}$.

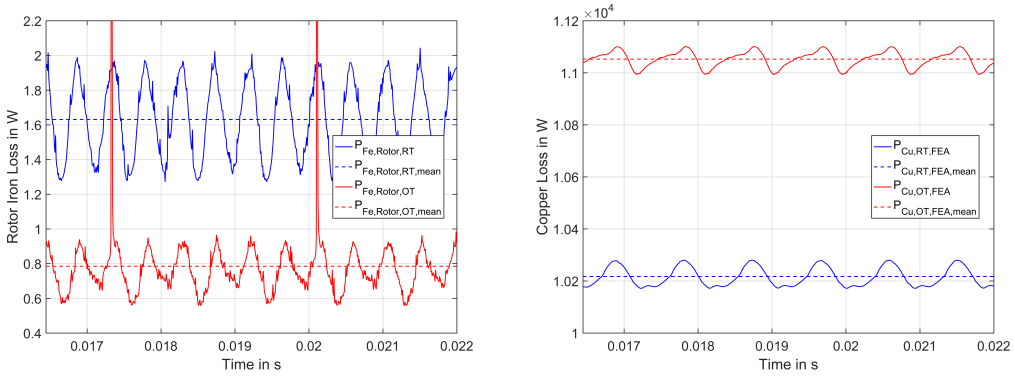

(a) (b)

Fig. 4.41: Losses acquired during simulation: $P_{\text{Fe,Rotor}}$ (a) and $P_{\text{Cu,Stator,total}}$ (b).

4.5 Loss Comparison

Table 4.10 and 4.11 sum up all obtained losses during simulation and post-processing. Fig. 4.42 shows the total losses, Fig. 4.43 shows rotor losses where the elimination of SRM rotor losses become obvious and Fig. 4.44 shows the dominating stator losses.

	Room Temperature			
Parameter	IM	Axially-layered R.	Solid Salient R.	Ring Salient R.
$P_{Cu,Stator,total}$	5158 W	1877 W	2272 W	10 217 W
$P_{Fe,Stator,total}$	29 W	18 W	32 W	60 W
$P_{Fe,Rotor}$	1.35 W	0.05 W	0.08 W	1.63 W
$P_{Cu,Rotor,layer}$	73 W	-	-	-
P_{total}	= 5261.35 W	= 1895.05 W	= 2304.08 W	= 10 278.63 W

Table 4.10: Loss comparison for room temperature

	Operating Temperature			
Parameter	IM	Axially-layered R.	Solid Salient R.	Ring Salient R.
$P_{Cu,Stator,total}$	4477 W	1888 W	2739 W	11 052 W
$P_{Fe,Stator,total}$	25 W	17 W	26 W	72 W
$P_{Fe,Rotor}$	2.84 W	0.05 W	0.06 W	0.78 W
$P_{Cu,Rotor,layer}$	201 W	-	-	-
P_{total}	= 4706.84 W	= 1905.05 W	= 2765.06 W	= 11 125.78 W

Table 4.11: Loss comparison for operating temperature

4.5 Loss Comparison

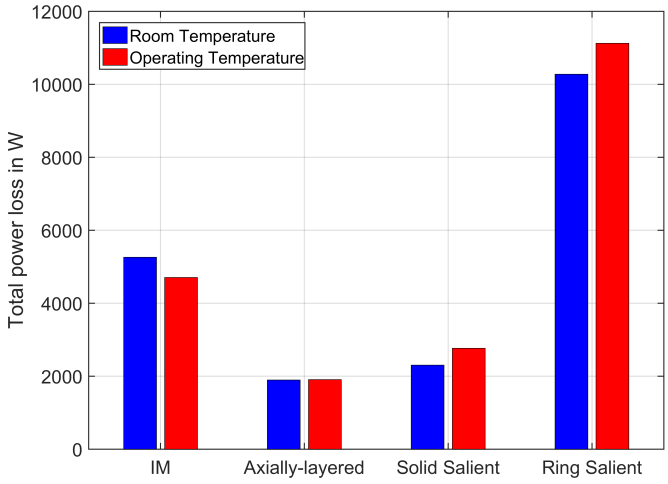

Fig. 4.42: Total power losses: Comparison at operating point of 1 Nm

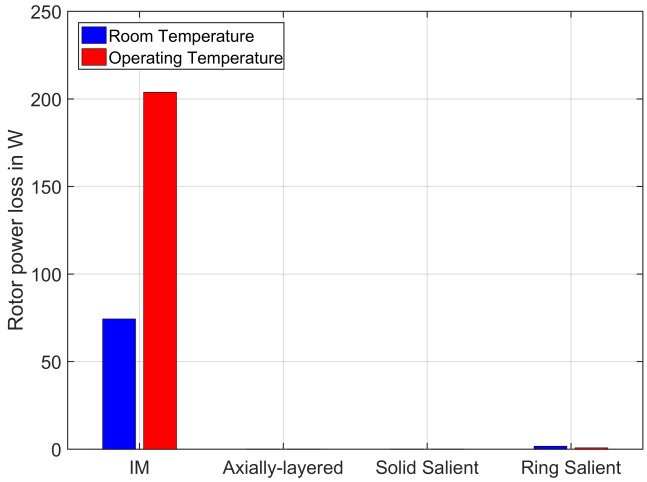

Fig. 4.43: Rotor losses: Comparison at operating point of 1 Nm

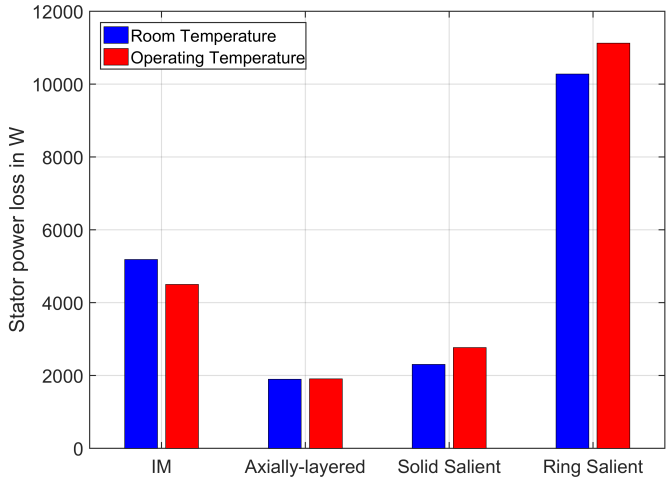

Fig. 4.44: Stator losses: Comparison at operating point of 1 Nm

5 Discussion

Analysis of Results

To ensure a useful base of comparison a fixed mechanical output power of around 1131 W was chosen. As such, the first requirement to reach the operating point of 1 Nm was met by all three investigated rotor shapes. However, the axially-layered and the solid salient rotor shapes show the most promising results in terms of the reduction of stator copper losses. As stated in Chapter 1, a higher current for the same torque output was expected but this only applies to the ring salient rotor shape. This is due to the fact that the important side condition of a large shaft diameter (as can be seen from the original rotor, Fig. 2.4) was ignored with the other two rotors and the shaft was reduced to a minimum. Generally, the larger shaft diameter is needed because the high-voltage line connected to the tube circuit runs through it. This implies that the shaft must give room to hold the voltage supply and the bearings (see Fig. 1.1). Nevertheless, the aim of this work was to offer a starting point for further research and to investigate the general feasibility of the rotor replacement. Subsequently, particular focus was placed on the special aspects of this drive including the large air gap, the high temperatures and the solid rotor construction.

Loss comparison

First of all the desirable elimination of rotor losses seems to be possible with all three rotor shapes. Furthermore, the stator loss comparison shows a significant reduction of copper losses for both the axially-layered and the solid salient rotor. This is in contrast to the ring salient rotor which shows doubled stator copper losses due to the increased phase current. However,

rotor losses are eliminated nonetheless and the similarity of the ring salient rotor shape to that of the original IM rotor would be, at the moment, the simplest replacement.

Suggested rotor improvements

The rotor shapes presented in this thesis represent a first suggestion and a starting point for further research and optimization processes involving the shape of the rotor and possible changes in the stator configuration. Therefore a brief overview on possible further research topics is given here.

Axially-layered rotor

The first suggestion is to optimize the number, location and width of the magnetically conductive layers. It can be pointed out that the magnetic layer in the middle of the rotor does not significantly contribute to the d-axis inductance due to the fact that the shaft interrupts and cuts through the entire middle layer significantly increasing the magnetic reluctance. Other important aspects to be investigated for this type of layered rotor are the mechanical stability, bonding of the alternating layers, general feasibility for the introduced vacuum application and, as already mentioned, the shaft diameter size.

Solid salient rotor

The magnetic flux density contour plot of this rotor shows a very obvious saturated part next to the shaft. An optimization could lead to an increased torque capability. Also the arclength and the radius of the cut out part (referring to the q-axis side of the rotor) offer a possible starting point for optimization.

Ring salient rotor

The idea of this rotor was to investigate the machine's behaviour while keeping the original shaft diameter and achieve the inductance difference by cutting out parts of the original rotor. It was possible to achieve the required mechanical output power although, unlike the shape of the rotor suggests, the greater inductance was achieved in q-axis direction. This is due to the fact that the very small ring on both sides of the rotor is highly saturated, increasing the magnetic reluctance significantly. Mechanical stability of this rotor shape has to be investigated as well as a possible reduction of the rotor shaft in favour of an increased amount of magnetizable material in the rotor.

Rotor of IM

Even though the emphasize of this work is on the investigated rotor shapes for a SRM configuration, taking a closer look at the investigated rotor of the IM shows a highly saturated rotor yoke. An optimization of the existing IM could include adapting the thickness of the rotor yoke and copper ring respectively.

Further Considerations

Changing stator geometry To decrease saturation in stator slots and stray inductance as it is visible for all motor configurations (Fig. 4.4, 4.14b, 4.26b and 4.37b), increasing the stator slot opening to increase magnetic flux yield could be investigated even for the existing IM.

Material Due to a lack of information about the materials in use modelling of the operating temperature shows some weaknesses as the exact change of electric resistivity could not be calculated. It was still possible to show the rough influence on current phase angle shift and torque production. A more thorough approach could include modelling a coupled magnetic-thermal study including applicable materials.

Loss Analysis The end winding leakage inductance as well as the stator iron core losses and their influence on the machines behaviour and the loss distribution were not considered during the simulation and could be included in a more detailed investigation.
3D effects, such as current distribution in the rotor end regions or stator end winding resistance and inductance that cannot be considered in a 2D-Analysis, especially when looking at the copper coated solid rotor, could be investigated by applying 3D-FEA.

Control Strategy Although the implemented control strategy was a secondary matter for this thesis, it might be possible to further reduce losses by implementing a current control ensuring a more favourable current angle β.

Appendix

Appendix A

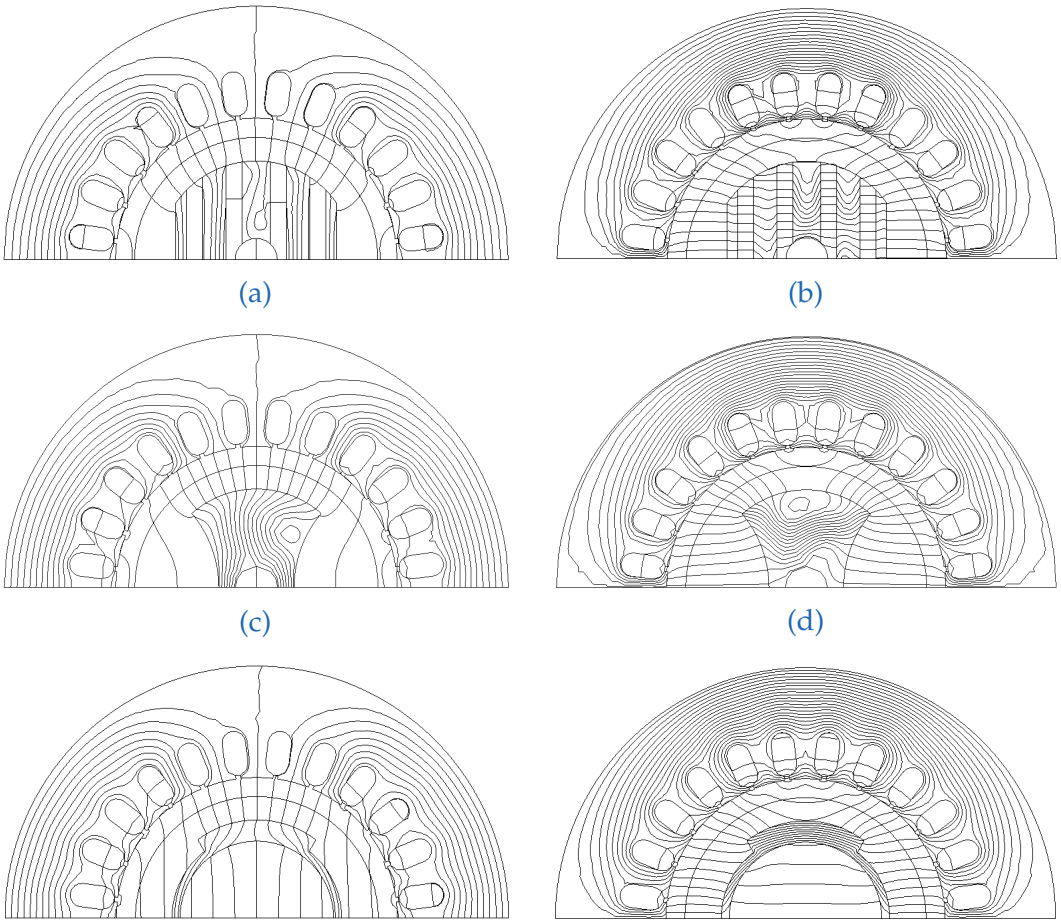

(a) (b) (c) (d) (e) (f)

Fig. .1: Magnetic flux lines at zero torque output. $\beta \approx 0°$, $I_q \approx 0\,A$ (a,c,e) and $\beta \approx 90°$, $I_d \approx 0\,A$ (b,d,f) for the axially-layered (a,b), solid salient (c,d) and ring salient (e,f) rotor

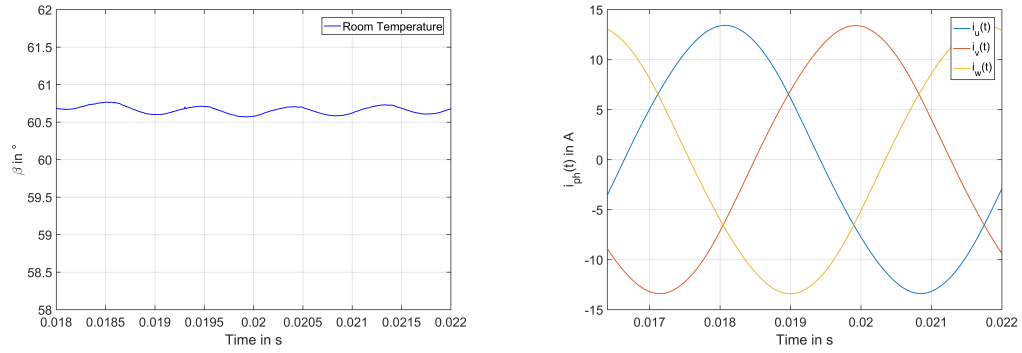

(a) (b)

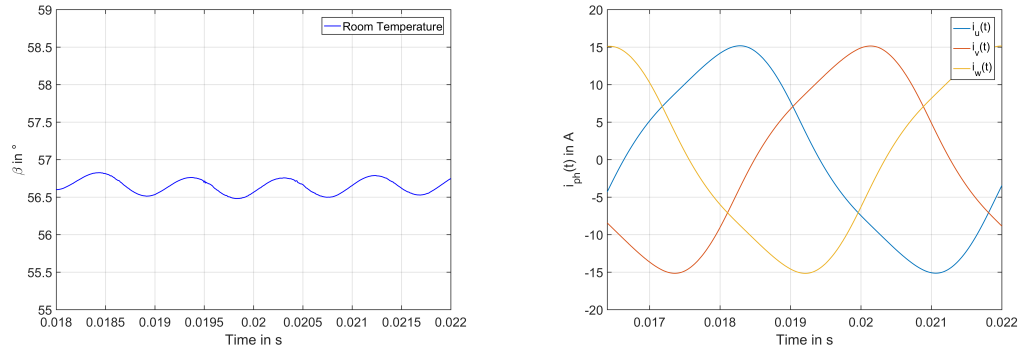

(c) (d)

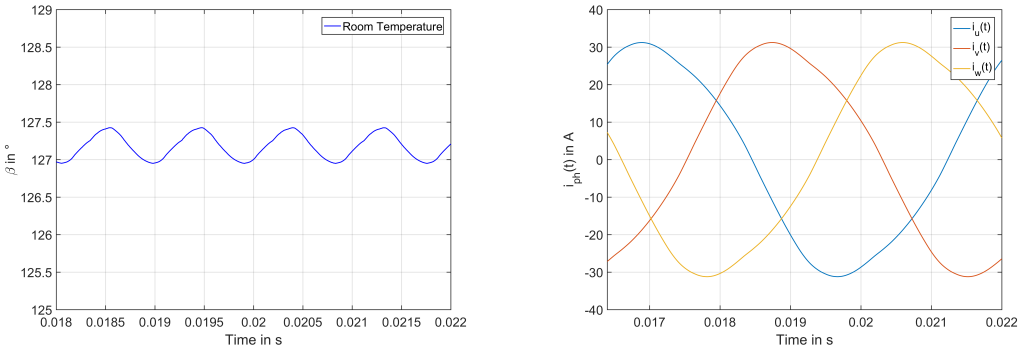

(e) (f)

Fig. .2: Variation of β over time for the operation point at room temperature (a,c,e) and corresponding (non sinusoidal) phase currents (b,d,f)

Bibliography

[1] H. Behner. (2005). Die Röntgenröhre im medizinischen Einsatzbereich, [Online]. Available: http://professor.wyndorps.reutlingen-university.de/Deutsch/Projektarbeit-Dateien/Roentgenroehre_11.pdf (visited on 03/01/2017).

[2] J. Hofman. (2010). The art of medical imaging: Philips and the evolution of medical X-ray technolgy, [Online]. Available: http://incenter.medical.philips.com/doclib/enc/fetch/2000/4504/577242/577256/588821/5050628/5313460/6391861/%5b04%5d_MM_54-1_Hofman.pdf%3fnodeid%3d6391873%26vernum%3d-2 (visited on 03/01/2017).

[3] R. Behling, *Modern Diagnostic X-Ray Sources: Technology, Manufacturing, Reliability*. Boca Raton, FL, USA: CRC Press, 2015.

[4] H. Hofmann and S. R. Sanders, "Synchronous reluctance motor/alternator for flywheel energy storage systems," in *Proceedings of the 1996 IEEE Power Electronics in Transportation Workshop*, IEEE, 1996, pp. 199–206.

[5] L. Xu, X. Xu, T. A. Lipo, and D. W. Novotny, "Vector control of a synchronous reluctance motor including saturation and iron loss," *IEEE Transactions on Industry Applications*, vol. 27, no. 5, pp. 977–985, 1991.

[6] T. A. Lipo, "Synchronous reluctance machines-a viable alternative for ac drives?" *Electric Machines and Power Systems*, vol. 19, no. 6, pp. 659–671, 1991.

[7] A. Boglietti and M. Pastorelli, "Induction and synchronous reluctance motors comparison," in *Industrial Electronics, 2008. IECON 2008. 34th Annual Conference of IEEE*, IEEE, 2008, pp. 2041–2044.

[8] M. Arefeen, M. Ehsani, and A. Lipo, "Sensorless position measurement in synchronous reluctance motor," *IEEE transactions on power electronics*, vol. 9, no. 6, pp. 624–630, 1994.

[9] M. H. Nagrial, "Developments of sensorless synchronous reluctance drive systems," in *Proceedings. IEEE International Multi Topic Conference, 2001. IEEE INMIC 2001. Technology for the 21st Century.*, 2001, pp. 104–110. DOI: 10.1109/INMIC.2001.995323.

[10] M.-T. Lin and T.-H. Liu, "Sensorless synchronous reluctance drive with standstill starting," *IEEE Transactions on Aerospace and Electronic Systems*, vol. 36, no. 4, pp. 1232–1241, Oct. 2000, ISSN: 0018-9251. DOI: 10.1109/7.892671.

[11] J. T. Bushberg, E. M. Leidholdt, A. J. Seibert, and J. M. Boone, *The essential physics of medical imaging*. Philadelphia, PA, USA: Lippincott Williams & Wilkins, 2002, pp. 97–99.

[12] G. A. Cervantes, *Technical Fundamentals of Radiology and CT*, ser. 2053-2563. Bristol, UK: IOP Publishing, 2016, ISBN: 978-0-7503-1212-7. DOI: 10.1088/978-0-7503-1212-7. [Online]. Available: http://dx.doi.org/10.1088/978-0-7503-1212-7.

[13] D. Dance, S. Christofides, and A. D. Maidment, "Diagnostic radiology physics: A handbook for teachers and students," 2014.

[14] *With kind permission of: Siemens healthineers, J. Deuringer (personal communication)*, 2017.

[15] J. G. Wright, "Design of a reluctance synchronous machine for traction motor applications using the finite element method," PhD thesis, Witwatersrand, Johannesburg, South Africa, 2011.

[16] C. Spargo, "Synchronous reluctance technology : Part I.," *MagNews.*, no. Winter, Jan. 2013. [Online]. Available: http://dro.dur.ac.uk/18579/.

[17] A. Binder, *Elektrische Maschinen und Antriebe*. Berlin, Germany: Springer, 2012.

[18] J. Pyrhönen, T. Jokinen, and V. Hrabovcová, *Design of Rotating Electrical Machines*. West Sussex, UK: John Wiley & Sons, Ltd, 2008.

[19] S. Tahi, R. Ibtiouen, and M. Bounekhla, "Design optimization of two synchronous reluctance machine structures with maximized torque and power factor," *Progress In Electromagnetics Research B*, vol. 35, pp. 369–387, 2011.

[20] J. R. Hendershot and T. J. E. Miller, *Design of brushless permanent-magnet machines*. Motor Design Books, 2010.

[21] S. Chapman, *Electric machinery fundamentals*. New York, NY, USA: Tata McGraw-Hill Education, 2005.

[22] T. Jokinen, "Losses of high-speed induction motors," *Prace-Instytut Elektrotechniki*, vol. 223, p. 71, 2004.

[23] *Rotating anode x-ray tube assembly*, Manual: Toshiba:vROTANODE E7252X/FX/GX, Toshiba Electron Tubes & Devices CO.,LTD.

[24] S. H. V. E. Corporation. (2017). Application notes - x-ray generators: Common x-ray tube failure modes, [Online]. Available: https://www.spellmanhv.com/en/Technical-Resources/Application-Notes-X-Ray-Generators/AN-02 (visited on 06/03/2017).

[25] J. Kolehmainen, "Synchronous reluctance motor with form blocked rotor," *IEEE Transactions on Energy Conversion*, vol. 25, no. 2, pp. 450–456, 2010.

[26] I. Boldea, Z. Fu, and S. Nasar, "Performance evaluation of axially-laminated anisotropic (ala) rotor reluctance synchronous motors," *IEEE Transactions on Industry Applications*, vol. 30, no. 4, pp. 977–985, 1994.

[27] H. Hofmann and S. R. Sanders, "High-speed synchronous reluctance machine with minimized rotor losses," *IEEE Transactions on Industry Applications*, vol. 36, no. 2, pp. 531–539, 2000.

[28] M.-I. Lamghari-Jamal, J. Fouladgar, E.-H. Zaim, and D. Trichet, "A magneto-thermal study of a high-speed synchronous reluctance machine," *IEEE Transactions on Magnetics*, vol. 42, no. 4, pp. 1271–1274, 2006.

[29] M. Zaim, "Application of a nonlinear complex finite element method to the design of solid rotor reluctance machines," *IEEE Transactions on Magnetics*, vol. 34, no. 5, pp. 3592–3595, 1998.

[30] A. Vagati, G. Franceschini, I. Marongiu, and G. Troglia, "Design criteria of high performance synchronous reluctance motors," in *Industry Applications Society Annual Meeting, 1992., Conference Record of the 1992 IEEE*, IEEE, 1992, pp. 66–73.

[31] G. Müller, K. Vogt, and B. Ponick, *Berechnung elektrischer Maschinen*. Weinheim, Germany: John Wiley & Sons, 2011.

[32] R. E. Betz, R. Lagerquist, M. Jovanovic, T. J. Miller, and R. H. Middleton, "Control of synchronous reluctance machines," *IEEE Transactions on Industry Applications*, vol. 29, no. 6, pp. 1110–1122, 1993.